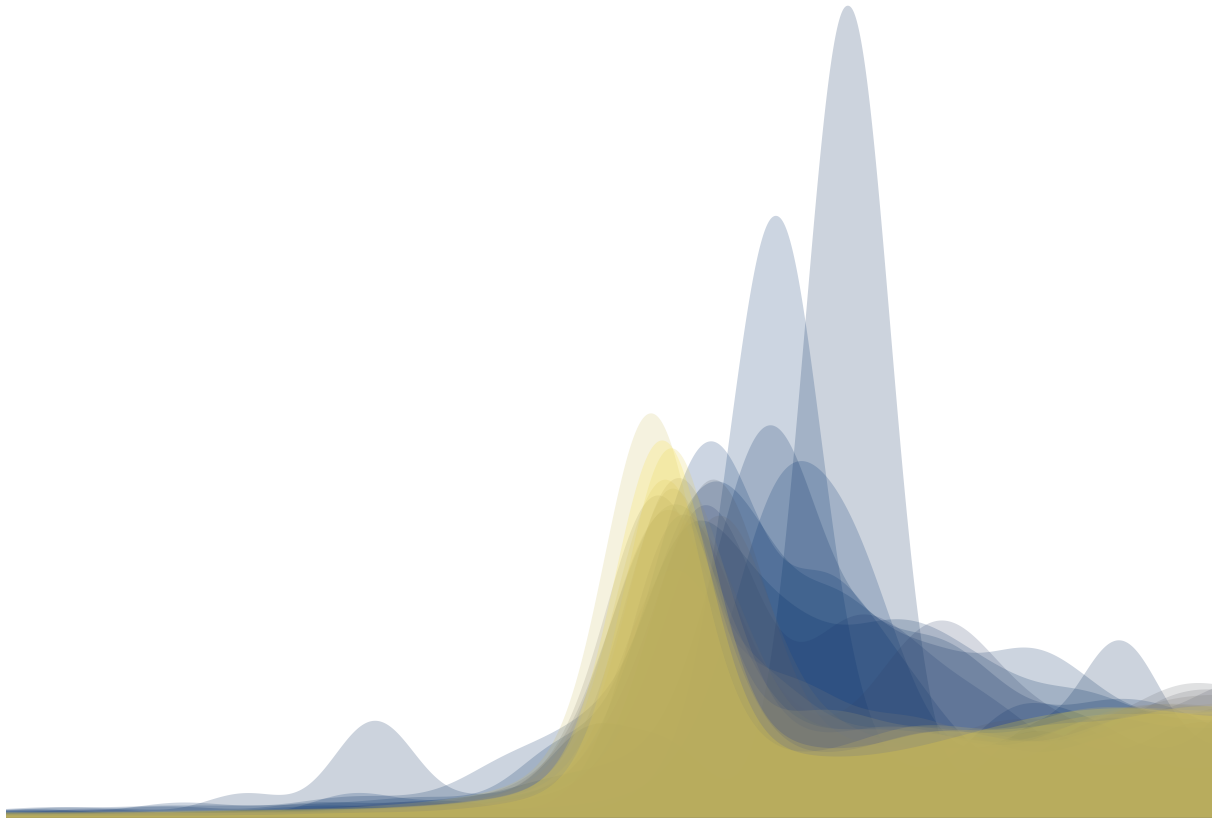




CHALMERS
UNIVERSITY OF TECHNOLOGY



Hot-carrier generation and transfer across nanoparticle-molecule interfaces

Master's thesis in Applied Physics

JAKUB FOJT

MASTER'S THESIS 2020

**Hot-carrier generation and transfer
across nanoparticle-molecule interfaces**

JAKUB FOJT



CHALMERS
UNIVERSITY OF TECHNOLOGY

Department of Physics
Division of Condensed Matter and Materials Theory
Computational Materials Research group
CHALMERS UNIVERSITY OF TECHNOLOGY
Gothenburg, Sweden 2020

Hot-carrier generation and transfer
across nanoparticle-molecule interfaces
JAKUB FOJT

© JAKUB FOJT, 2020.

Examiner and supervisor: Paul Erhart, Department of Physics
Supervisor: Tuomas Rossi, Department of Physics

Master's Thesis 2020
Department of Physics
Division of Condensed Matter and Materials Theory
Computational Materials Research group
Chalmers University of Technology
SE-412 96 Gothenburg
Telephone +46 31 772 1000

Cover: Photoabsorption spectra of Ag nanoparticles of size up to 586 atoms

Typeset in L^AT_EX
Printed by Chalmers Reproservice
Gothenburg, Sweden 2020

JAKUB FOJT

Department of Physics

Chalmers University of Technology

Abstract

Metallic nanoparticles are important materials for emerging sensing and catalysis technologies. Their special properties stem from the presence of a localized surface plasmon resonance (LSPR) mode that can couple to visible light. The LSPR causes the nanoparticle to scatter and absorb more light at frequencies that match the plasmon energy. The plasmon excitation has a lifetime of a few femtoseconds before it dephases into electrons and holes with a strongly athermal energy distribution. In this thesis, time-dependent density functional theory has been employed to study these phenomena in Ag nanoparticles. In the first part of this thesis, the photoabsorption spectra were systematically calculated for a series of Ag nanoparticles. The particles were between $N = 13$ and 586 atoms in size and included both regular and irregular shapes. The main findings are that the LSPR peak frequency depends linearly on $N^{-1/3}$ for $N \geq 201$.

When a plasmon forms in a nanoparticle in the vicinity of a molecule it may dephase into a transition of an electron from the nanoparticle to the LUMO state of the molecule, or from the HOMO state of the molecule to an unoccupied state in the nanoparticle. These processes are termed direct hot-electron transfer and direct hot-hole transfer, respectively. In the second part of the thesis, a systematic study was carried out in which a CO molecule was placed at different distances from the nanoparticle, and the system was excited with a laser pulse. The results indicate that for this system direct hot-electron transfer happens with a probability of around 1% and is only weakly dependent on the molecule-nanoparticle separation until it decays to zero at large distances. Meanwhile, the probability of hot-hole transfer is between 0.2 and 0.3% at a distance of 1.8 Å and decays monotonically. Contributing factors to the differences are that the molecular LUMO state is sufficiently close to the Fermi level for hot-electron transfer to occur, while only hybridized tails of the HOMO state satisfy the corresponding requirement for hot-hole transfer. The most important criterion for transfer to occur is an alignment in energy between the nanoparticle and molecular densities of state.

Keywords: Hot-carriers, localized surface plasmon resonance, time-dependent density functional theory

Acknowledgements

I would like to thank my examiner and supervisor Prof. Paul Erhart for the opportunity to write this thesis and your guidance along the way. Your knowledge of the field has been an inspiration to me in pursuing academics, and I look forward to beginning my doctoral studies with you as my supervisor.

My sincere thanks also go to my supervisor Dr. Tuomas Rossi for your help answering big and small questions, and your feedback on the drafts of this thesis. Your help troubleshooting practical computational matters has spared me from many headaches.

Thank you, Victor Rosendal, for your opposition at my thesis defence, as well as the coffee breaks and rewarding discussions about our respective projects.

Finally I would like to thank my family for their encouragement of my studies, my friends who have made the five years at Chalmers an enjoyable experience, and Isabel Vrethed Tidekrans who has supported me at home.

Jakub Fojt, Gothenburg, August 2020

Contents

List of Figures	xi
1 Introduction	1
1.1 Background	1
1.2 Aim	2
1.2.1 Previous work	2
1.2.2 Specific questions	3
1.2.3 Limitations	3
2 Theory	5
2.1 The many-body problem	5
2.1.1 Born-Oppenheimer approximation	6
2.2 Density functional theory	6
2.2.1 Kohn-Sham approach	7
2.2.1.1 Local density approximation	8
2.2.1.2 Perdew-Burke-Enzerhof	8
2.2.1.3 GLLB-SC	9
2.2.1.4 DFT+U	9
2.3 Time-dependent density functional theory	9
2.3.1 Fundamental theory	10
2.3.2 Adiabatic approximation	10
2.3.3 Photoabsorption in the linear response regime	11
3 (TD)DFT in practice	13
3.1 Calculating the ground state with KS-DFT	14
3.1.1 The self-consistent algorithm	15
3.1.2 Occupation number smearing	16
3.1.3 Density of states	16
3.1.4 The LCAO basis set	16
3.1.5 Ground state properties of Na and Ag chains	17
3.2 Calculating optical properties with TDDFT	19
3.2.1 Calculating observables	20
3.2.2 Optical properties of Na and Ag chains	22
4 Size dependence of photoabsorption spectra	25
4.1 Selected structures	25
4.2 Size dependence of energies	26

4.3	Calculated spectra	27
4.4	Choice of numerical parameters	31
4.5	Summary	33
5	Hot-carrier transfer	35
5.1	Hot-carrier dynamics for the bare NP	37
5.2	Hot-carrier transfer across CO-NP interface	39
5.2.1	Binding energies as a function of distance	39
5.2.2	Projected densities of state	42
5.2.3	Hot-carrier distributions after plasmon decay	44
5.2.3.1	Direct hot-electron transfer	47
5.2.3.2	Direct hot-hole transfer and other processes	47
5.3	Generalization and future considerations	51
5.3.1	Probe orbital approach	52
5.4	Summary	56
6	Conclusion	57
	Bibliography	59

List of Figures

3.1	A linear chain of eight atoms	13
3.2	Self-consistent algorithm for finding the ground state density	15
3.3	Densities of state and isosurfaces of selected KS orbitals for Na ₈ in finite difference and LCAO mode	18
3.4	Densities of states for Na and Ag chains with finite difference/LCAO mode and LDA/GLLB-SC functional	18
3.5	Relevant external potentials in the time and frequency domains	20
3.6	The photoabsorption spectrum in the chain axis direction for the Na ₈ and Ag ₈ atom chains	23
3.7	Transition contribution maps for Na ₈ and Ag ₈	23
3.8	Isosurfaces of induced densities $\delta n(\mathbf{r}, \omega)$ at the LSPR	24
4.1	Classification of some of the NPs studied in this chapter	26
4.2	Energies of NPs for EAM potential and DFT data	27
4.3	Photoabsorption spectra for selected NPs	28
4.4	Direction averaged spectra of NPs as a function of $N^{-1/3}$	29
4.5	The LSPR energy and intensity versus $N^{-1/3}$	30
4.6	Convergence check for the parameters v, h and dt	32
5.1	Density of states for the bare Ag ₂₀₁ RTO	36
5.2	Photoabsorption spectrum of the bare Ag ₂₀₁ RTO	36
5.3	TCMs $M(t, \varepsilon_o, \varepsilon_u)$ to the transition probability $P_{ia}(t)$	38
5.4	Projection of the hot-carrier distribution $M(t, \varepsilon_o, \varepsilon_u)$ at $t = 30$ fs on the electron and hole energy axes $M^h(t, \varepsilon_o)$ and $M^e(t, \varepsilon_u)$	38
5.5	The four considered sites of CO adsorption	39
5.6	Binding energy curves for the four adsorption configurations	41
5.7	Binding energy curves for strained NPs in the [111] on-top configuration	41
5.8	Molecular PDOS for the [111] on-top site with GLLB-SC functional	43
5.9	Molecular PDOS for the [111] on-top site and corner site, with both xc -functionals	44
5.10	Probabilities of hot-carrier transfer processes as a function of the separation between the NP and CO molecule	46
5.11	GLLB-SC [111] on-top site hot-hole and hot-electron distributions	46
5.12	GLLB-SC [111] on-top site hot-carrier distributions for the direct hot- electron transfer process in relation to NP and molecular PDOS	48
5.13	GLLB-SC [111] on-top site joint density of states related to the direct hot-electron transfer process	48

5.14	GLLB-SC [111] on-top site hot-carrier distributions for the direct hot-hole transfer process in relation to NP and molecular PDOS	50
5.15	GLLB-SC [111] on-top site joint density of states related to the direct hot-hole transfer process	50
5.16	Schematic drawing of conditions required for hot-electron transfer . . .	51
5.17	The potential used to implement the probe orbital	52
5.18	PDOS of the probe orbital $D^{\text{probe}}(\varepsilon)$ for the [111] on-top site with the PBE+U <i>xc</i> -functional	53
5.19	Probability of the direct hot-electron transfer process as a function of the separation between the NP and probe	54
5.20	Probe orbital [111] on-top site hot-carrier distributions for the direct hot-electron transfer process in relation to NP and probe PDOS . . .	55
5.21	Probe orbital [111] on-top site joint density of states related to the direct hot-electron transfer process	55

1

Introduction

1.1 Background

Metallic nanoparticles (NPs) are key materials in emerging sensing^{1,2}, catalysis³ and cancer treatment⁴ technologies. They are being used to develop biosensors capable of detecting single antibodies¹ and hydrogen sensors for detecting dangerous leaks². When they are illuminated by light of solar intensity, NPs have been demonstrated to act as room-temperature catalysts for commercially important reactions, potentially leading to more efficient catalysis with fewer unwanted byproducts³. At the present, catalysis is used to reduce pollutants from vehicles and is the foundation of much of the chemical industry. From this perspective the development of catalysis is important.

The optical properties of metallic NPs differ from bulk materials because of the presence of localized surface plasmons in NPs⁵. In this context, plasmons are oscillations of the density of the valence electrons of the metal. The valence electrons are displaced by an externally applied electric field until enough charge accumulates at the NP surface to counteract the field. If the field is alternating, the electrons will oscillate with the field. The phenomenon where the field and electron density oscillations resonate is called the localized surface plasmon resonance (LSPR). The scattering and absorption of light is enhanced at the LSPR. For several transition metals the LSPR occurs at an optical frequency. The effect is visible to the naked eye, for example in stained glass church windows where yellow colors may come from embedded silver NPs⁵.

NPs are especially attractive for applications as they have a high optical absorption cross section at the LSPR frequency^{6,7}, and the LSPR frequency is dependent on the particle size, shape, chemical composition, and environment⁸. There are thus many parameters that can be tuned to engineer NPs to a specific problem. For sensing applications one can monitor the LSPR and correlate changes in peak position, width or intensity to changes in the environment or the particle itself.^{2,9}

The LSPR opens up further possibilities in catalysis. Processes used in industry today rely on the presence of a catalyst that lowers reaction barriers, which are overcome by thermal energy^{10,11}. With plasmonic NPs as catalysts, charge carriers (electrons or holes) formed after the decay of a plasmon may transiently populate orbitals of the reactant, driving the catalytic reaction^{10,11}. The literature suggests two different variants of this process; an *indirect* transfer process where charge carriers are formed in the nanoparticle and transferred to the reactant, and a *direct* process

where the plasmon in the nanoparticle directly decays into unoccupied orbitals of the reactant^{3,10}. It has been proposed that the latter is more efficient and selective¹⁰ (i.e. provides more control over byproducts). Currently there are open questions regarding the ratio between the direct and indirect processes.

Plasmonically driven catalysis has the potential to become commercially viable if it presents a significant advantage over the industry standard processes, such as high selectivity or high efficiency at low temperatures. It is believed that the promotion of the direct transfer process over the indirect could achieve this¹⁰. As the two processes happen on the same time scales they are experimentally difficult to distinguish. This has motivated computational studies^{12–14} using time-dependent density functional theory^{15,16} (TDDFT).

1.2 Aim

The aim of this thesis is to explore a few aspects of the optical and photocatalytical properties of Ag NPs from first principles. Computations are performed within the framework of TDDFT, which is introduced in chapter 2. Technical details of how the theory is implemented in computations are described in chapter 3, while illustrating the LSPR in an example system.

The thesis follows two tracks, each related to one of the previous studies by Kuisma *et al.*¹⁷ and Kumar *et al.*¹⁴. Similar to the study by Kuisma *et al.*¹⁷, chapter 4 explores the dependence of the photoabsorption spectrum on the NP size. While Kuisma *et al.* have calculated spectra for a few NPs of regular shapes, this thesis covers NP of regular and irregular shapes in a range of sizes. Following the study by Kumar *et al.*¹⁴, the probabilities of hot-carrier transfer processes across the NP and CO molecule interface are calculated in chapter 5. While Kumar *et al.* have studied the CO at an equilibrium distance from the NP, quantities in this thesis are calculated as functions of distance.

1.2.1 Previous work

Kuisma *et al.*¹⁷ have calculated the absorption spectra of the four icosahedral NPs Ag₅₅, Ag₁₄₇, Ag₃₀₉ and Ag₅₆₁. They found a redshift of the LSPR with increasing NP size.

Rahm and Erhart¹⁸ have determined thermodynamically stable shapes of NPs as a function of the number of constituent atoms. They have imposed constraints on the shapes such that they are similar to some motif, *e.g.* an icosahedron or truncated octahedron. Structures generated by Rahm and Erhart make up the sequence of NPs studied in chapter 4.

Kumar *et al.*¹⁴ have studied the initial step of photocatalysis of an adsorbate CO molecule on Ag₁₄₇ by simulating a process of laser illumination, plasmon formation and plasmon decay with TDDFT. They show that within 30 fs the plasmon has decayed, and a small fraction of it has transferred into the CO molecule (which makes up the direct transfer process). For three different adsorption sites Kumar *et al.* calculated the probabilities of the direct transfer to fall between 0.9% and 2.0%.

1.2.2 Specific questions

Specific questions answered in this thesis are:

- How do ground state energies and photoabsorption spectra vary as a function of NP size, for a sequence of truncated octahedron-like NPs?
- What is the distance and adsorption site dependence of the direct electron/hole transfer processes probabilities for $\text{Ag}_{201}+\text{CO}$?
- What predictions in terms of hot-carrier transfer can be made for other systems and how can the process probabilities be affected?

1.2.3 Limitations

The investigations in this thesis are carried out with an explicit time propagation scheme in TDDFT. This limits the time spans of processes that can be covered with a reasonable computational effort to approximately 30 fs. This is the time scale of plasmon dynamics and hot-carrier generation. However molecular dynamics and bond breaking happen on longer time scales and are computationally inaccessible with the present methodology.

The TDDFT data is analyzed within a linear response framework. We assume that the driving optical fields are sufficiently weak for a linear response. Thus non-linear effects from very strong light are not covered in this thesis.

2

Theory

This chapter covers the relevant basics of density functional theory (DFT) and time dependent density functional theory (TDDFT). A more complete description of the former can be found in the textbook by Martin¹⁹ and of the latter in the compendium by Ullrich and Yang¹⁶. For simplicity explicit spin dependence is omitted from the equations and Hartree atomic units are used. In Hartree atomic units the electron mass m_e , elementary charge e , and reduced Planck constant \hbar are unity and are conveniently omitted from the equations.

2.1 The many-body problem

In quantum mechanics all systems are governed by the time-dependent Schrödinger equation

$$i\frac{d\Psi(t)}{dt} = \hat{H}\Psi(t) \quad (2.1)$$

where $\Psi(t)$ is the (many-body) wave function that describes the *state* of the system and \hat{H} the Hamiltonian operator that defines it. If the Hamiltonian is independent of time one can formulate the time-independent Schrödinger equation

$$\hat{H}\Psi_n = E_n\Psi_n. \quad (2.2)$$

It is an eigenvalue equation, where the eigenstates Ψ_n are stationary states of the time-dependent Schrödinger equation, and the eigenvalues E_n the corresponding energies.

The Hamiltonian of any system consisting of electrons and nuclei can be divided into a kinetic part \hat{T} and potential part \hat{V} and written

$$\hat{H} = \hat{T} + \hat{V} \quad (2.3)$$

$$\hat{T} = -\sum_i \frac{1}{2}\nabla_i^2 - \sum_I \frac{1}{2M_I}\nabla_I^2 \quad (2.4)$$

$$\hat{V} = -\frac{1}{2}\sum_{i,I} \frac{Z_I}{|\mathbf{r}_i - \mathbf{R}_I|} + \sum_{i \neq j} \frac{1}{|\mathbf{r}_i - \mathbf{r}_j|} + \frac{1}{2}\sum_{I \neq J} \frac{Z_I Z_J}{|\mathbf{R}_I - \mathbf{R}_J|}. \quad (2.5)$$

Here, we use the convention that lower case indexes refer to electrons and capital indexes to atomic nuclei. The kinetic operator is a sum of second derivatives in the coordinates of each electron ∇_i^2 and nucleus ∇_I^2 while the potential operator depends on the coordinates of electrons \mathbf{r}_i and nuclei \mathbf{R}_I . M_I and Z_I are the mass and electronic charge of each nucleus I , respectively. As Hartree atomic units are

used the electron mass is 1 and electron charge -1. The wave function Ψ is a function of the coordinates of the electrons and nuclei (and time for the time-dependent Schrödinger equation)

$$\Psi = \Psi(\{\mathbf{R}_I\}_I, \{\mathbf{r}_i\}_i, t). \quad (2.6)$$

2.1.1 Born-Oppenheimer approximation

Since the mass of any nucleus is much larger than the mass of an electron $M_I \gg 1$ it is reasonable to assume that the nuclei are motionless in short time scales. This is called the *Born-Oppenheimer* approximation. The kinetic energy of the nuclei is then zero and nucleus-nucleus interaction energy which is the third term of (2.5) is constant

$$E_{\text{II}} = \frac{1}{2} \sum_{I \neq J} \frac{Z_I Z_J}{|\mathbf{R}_I - \mathbf{R}_J|}. \quad (2.7)$$

The Born-Oppenheimer Hamiltonian consists of the kinetic energy of the electrons \hat{T} and the potential energy of the interacting electrons \hat{V}_{int} . Additionally the electrons are under the influence of an external potential \hat{V}_{ext} from the nuclei and possibly other sources.

$$\hat{H} = \hat{T} + \hat{V}_{\text{int}} + \hat{V}_{\text{ext}} + E_{\text{II}} \quad (2.8)$$

$$\hat{T} = - \sum_i \frac{1}{2} \nabla_i^2 \quad (2.9)$$

$$\hat{V}_{\text{ext}} = - \frac{1}{2} \sum_{i,I} \frac{Z_I}{|\mathbf{r}_i - \mathbf{R}_I|} \quad (2.10)$$

$$\hat{V}_{\text{int}} = \sum_{i \neq j} \frac{1}{|\mathbf{r}_i - \mathbf{r}_j|} \quad (2.11)$$

As the kinetic operator (2.9) and electron-electron interaction operator (2.11) always are on the same form, we can say that all electronic systems are defined by the external potential (from nuclei and externally applied fields) acting on it.

The Born-Oppenheimer Hamiltonian (2.8) and time-dependent or independent Schrödinger equation (2.1), (2.2) describe the behavior of electrons, but these equations are too complex to solve in practice. The main obstacle is that Ψ is a function of $3N$ spatial coordinates. To represent it numerically, say on a grid of 10 points in each direction, would require 10^{3N} grid points. The exponential scaling of the number of required points on N makes calculations practically impossible for systems with more than a few electrons, and calls for the need of alternative methods such as DFT.

2.2 Density functional theory

Density functional theory (DFT) is based on the formal proof by Hohenberg and Kohn²⁰ that all properties of an electronic system are determined by the electron density $n(\mathbf{r})$ of its ground state. Furthermore $n(\mathbf{r})$ is uniquely determined as the

function that minimizes a universal energy functional $E[n]$. DFT is an exact reformulation of quantum mechanics with the advantage that it concerns a function of only three spatial variables for any system, while in the Schrödinger formulation the many-body wave function depends on three coordinates per particle in the system. DFT makes computational approaches tractable for systems consisting of more than a few electrons.

The challenge of DFT is that the general expression for the universal functional is not known. There are various approximate functionals; those relevant for this thesis are described in this section.

2.2.1 Kohn-Sham approach

One of the difficulties in finding an expression for the functional $E[n]$ is the contribution of the kinetic energy (2.9). In the Schrödinger formulation of quantum mechanics it is given by gradients (in the coordinates of each electron) of the many-body wave function. This quantity cannot be simply extracted from the ground state density. To circumvent this problem, Kohn and Sham²¹ proposed an alternative formulation of the problem. They assumed that there is an *auxiliary system* of N non-interacting electrons in an *effective potential* $v_{\text{eff}}(\mathbf{r})$, that has the same density as the true system. Since the particles are independent they are described by N wave functions $\phi_i(\mathbf{r})$ (referred to as the KS wave functions or KS orbitals), with the density $n(\mathbf{r}) = \sum_{i=1}^N |\phi_i(\mathbf{r})|^2$. In the Kohn-Sham formulation the universal energy functional is written in the form

$$E[n] = T_s[n] + \int d\mathbf{r} V_{\text{ext}}(\mathbf{r})n(\mathbf{r}) + \frac{1}{2} \int d\mathbf{r} d\mathbf{r}' \frac{n(\mathbf{r})n(\mathbf{r}')}{|\mathbf{r} - \mathbf{r}'|} + E_{\text{II}} + E_{\text{xc}}[n], \quad (2.12)$$

where the five terms are described in the following paragraph. The first term $T_s[n] = -1/2 \sum_i \int d\mathbf{r} \phi_i^*(\mathbf{r}) \nabla^2 \phi_i(\mathbf{r})$ is the kinetic energy of the auxiliary system. The second term is the external energy of the electron density $n(\mathbf{r})$ interacting with the external potential $V_{\text{ext}}(\mathbf{r})$ from the atomic nuclei (and possibly an additional external electric field). The third term is the Hartree energy and represents the classical electrostatic energy. It can be understood as the energy of the density interacting with the electric field the density creates. The fourth term E_{II} is the Coulomb energy from the nuclei interacting with each other. E_{II} and $V_{\text{ext}}(\mathbf{r})$ depend only on the positions and types of atomic nuclei, and the externally applied potential. The remaining energy contributions are grouped into the fifth term $E_{\text{xc}}[n]$, called the *exchange-correlation* energy. With the functional $E[n]$ on this form, E_{II} and $V_{\text{ext}}(\mathbf{r})$ are the quantities that define the system, while all other quantities are universal.

The theory has been reformulated so that $E_{\text{xc}}[n]$ is the only unknown. Given an exact expression for $E_{\text{xc}}[n]$, and assuming the validity of the KS Ansatz, the theory is exact. In practice the exchange-correlation energy functional needs to be approximated, and the approximations relevant for this thesis are described later in this section. Usually this energy is further treated as *exchange* and *correlation* separately. The former refers to the Pauli exclusion effect that electrons of the same spin cannot be in the same position. The latter refers to a screening interaction; the probability of finding an electron near another is decreased as it is energetically

unfavorable. The correlation energy is especially important for electrons of opposite spin, as they are not required to avoid each other due to Pauli exclusion.

By minimizing the energy functional (2.12) using the variational principle one can show that the auxiliary system obeys the Schrödinger-like equation

$$\left(-\frac{1}{2}\nabla^2 + v_{\text{eff}}[n](\mathbf{r})\right)\phi_i(\mathbf{r}) = \varepsilon_i\phi_i(\mathbf{r}). \quad (2.13)$$

The KS wave functions $\phi_i(\mathbf{r})$ are the eigenfunctions corresponding to the N lowest eigenvalues of (2.13). The effective potential $v_{\text{eff}}[n](\mathbf{r})$ can be expressed in terms of functional derivatives

$$v_{\text{eff}}[n](\mathbf{r}) = v_{\text{ext}}(\mathbf{r}) + v_{\text{Hartree}}[n](\mathbf{r}) + v_{\text{xc}}[n](\mathbf{r}) \quad (2.14)$$

$$v_{\text{ext}}(\mathbf{r}) = \frac{\delta}{\delta n(\mathbf{r})} \int d\mathbf{r}' V_{\text{ext}}(\mathbf{r}')n(\mathbf{r}') = V_{\text{ext}}(\mathbf{r}) \quad (2.15)$$

$$v_{\text{Hartree}}[n](\mathbf{r}) = \frac{\delta}{\delta n(\mathbf{r})} \frac{1}{2} \int d\mathbf{r}' d\mathbf{r}'' \frac{n(\mathbf{r}')n(\mathbf{r}'')}{|\mathbf{r}' - \mathbf{r}''|} = \frac{1}{2} \int d\mathbf{r}' \frac{n(\mathbf{r}')}{|\mathbf{r} - \mathbf{r}'|} \quad (2.16)$$

$$v_{\text{xc}}[n](\mathbf{r}) = \frac{\delta E_{\text{xc}}[n]}{\delta n(\mathbf{r})}. \quad (2.17)$$

2.2.1.1 Local density approximation

In the local density approximation (LDA)^{22–24} the exchange-correlation functional is taken to be the same as for the homogeneous electron gas. It is a local functional, meaning it is on the form

$$E_{\text{xc}}^{\text{LDA}}[n] = \int d\mathbf{r} n(\mathbf{r})[\epsilon_{\text{x}}(n(\mathbf{r})) + \epsilon_{\text{c}}(n(\mathbf{r}))], \quad (2.18)$$

where the exchange and correlation energy densities $\epsilon(n(\mathbf{r}))$ are functions of the density at one point in space. The exchange has an exact analytic expression^{22,23}, and the correlation is fitted to Monte Carlo calculations²⁴.

Since the LDA is based on a homogeneous electron gas it can be expected to work best for nearly-free-electron metals, such as Na, and worst for isolated atoms and molecules where the electron density continuously approaches zero. Comparisons of LDA with small systems such as the H atom or H₂ molecule for which exact solutions are known shows that it tends to underestimate exchange energies and overestimate correlation energies. Because the errors in exchange and correlation tend to cancel, the total error is not too large even for isolated systems¹⁹.

2.2.1.2 Perdew-Burke-Enzerhof

The Perdew-Burke-Enzerhof (PBE) functional²⁵ belongs to the generalized gradient approximation (GGA) class of functionals. The idea behind GGAs is to extend the energy density in (2.18) to depend also on gradients of the density

$$E_{\text{xc}}^{\text{GGA}}[n] = \int d\mathbf{r} n(\mathbf{r})\epsilon_{\text{xc}}(n(\mathbf{r}), \nabla n(\mathbf{r}), \dots). \quad (2.19)$$

The PBE functional has been developed to improve total energies for isolated systems, without describing systems of slowly varying density worse²⁵.

2.2.1.3 GLLB-SC

In contrast to LDA and PBE, which are functionals for the energy $E_{xc}[n]$, the Gritsenko-van Leeuwen-van Lenthe-Baerends (GLLB)²⁶ functional is an expression for $v_{xc}[n](\mathbf{r})$. It is a potential functional, without a well-defined total energy. The most important feature of the GLLB functional is that it incorporates a discontinuity in the exchange-correlation potential at integer occupation numbers

$$\Delta_{xc} = \lim_{\delta \rightarrow 0} v_{xc}(\mathbf{r}, N + \delta) - v_{xc}(\mathbf{r}, N - \delta) \neq 0 \quad (2.20)$$

which LDA and PBE lack. It can be shown that the discontinuity must be a feature of the true exchange-correlation functional²⁷. The discontinuity is important to obtain accurate band gaps.

The GLLB-SC functional²⁸ is a modification of GLLB with better description of solids and correlation. It greatly improves the location of the d-band in noble metals, which is important for plasmonic systems composed of these metals^{17,29,30}.

2.2.1.4 DFT+U

The DFT+U method is a way to compensate for interactions between localized electrons which are underestimated by xc -functionals such as LDA or PBE^{19,31}. The correction is typically applied to electrons with a certain angular momentum quantum number l , typically d- or f-electrons³¹, and its strength specified by a Hubbard parameter U . In this thesis, the implementation follows Dudarev *et al.*³¹

$$E_{\text{DFT+U}} = E_{xc}^{\text{LDA/PBE}} + \sum_a \frac{U}{2} \text{Tr}(\rho^{a,l} - \rho^{a,l} \rho^{a,l}). \quad (2.21)$$

Here the sum runs over all atoms a and $\rho^{a,l}$ is a occupation matrix for atom a and quantum number l . In this thesis the Hubbard +U correction is applied to d-electrons of Ag with the PBE functional, to get a similar description as with GLLB-SC. This is referred to as PBE+U.

2.3 Time-dependent density functional theory

In this thesis TDDFT is used to calculate the optical properties of systems. This is done by considering a time-dependent external potential

$$v_{\text{ext}}(\mathbf{r}, t) = \begin{cases} v_{\text{ext}}^{(0)}(\mathbf{r}) & , t < 0 \\ v_{\text{ext}}^{(0)}(\mathbf{r}) + v_1(\mathbf{r}, t) & , t \geq 0 \end{cases} \quad (2.22)$$

which is initially static. At time $t = 0$ the potential $v_1(\mathbf{r}, t)$ of an optical field is turned on.

In this thesis, time-dependent functions and their Fourier transforms are denoted by the same letter. They are distinguished by the dependence on time t or frequency ω , *e.g.*

$$f(\mathbf{r}, \omega) = \int_{-\infty}^{\infty} dt f(\mathbf{r}, t) e^{i\omega t}. \quad (2.23)$$

2.3.1 Fundamental theory

While DFT describes systems in their ground state under the influence of a potential constant in time, TDDFT extends the theory to describe systems in an explicitly time-dependent potential. Analogously to the proof by Hohenberg and Kohn²⁰, Runge and Gross¹⁵ show that there is a one-to-one correspondence between the external potential acting on a system and the time-dependent density of the system. Formally, the external potential at any given time is a functional of the density *at all previous times* and the many-body wave function Ψ_0 of the system at $t = 0$.

Analogously to the Kohn-Sham equations (2.13) and (2.14) one assumes that the time-dependent KS states make up the density $\sum_{i=1}^N |\phi_i(\mathbf{r}, t)|^2 = n(\mathbf{r}, t)$ and obey the time-dependent Schrödinger-like equation

$$\left(-\frac{1}{2}\nabla^2 + v_{\text{eff}}[n](\mathbf{r}, t)\right)\phi_i(\mathbf{r}, t) = i\frac{\partial}{\partial t}\phi_i(\mathbf{r}, t). \quad (2.24)$$

given some initial conditions on the KS wave functions $\phi_i(\mathbf{r}, 0) = \phi_i^{(0)}(\mathbf{r})$. Analogously to the time-independent case

$$v_{\text{eff}}[n](\mathbf{r}, t) = v_{\text{ext}}(\mathbf{r}, t) + v_{\text{Hartree}}[n](\mathbf{r}, t) + v_{\text{xc}}[n](\mathbf{r}, t) \quad (2.25)$$

$$v_{\text{Hartree}}[n](\mathbf{r}, t) = \frac{1}{2} \int d\mathbf{r}' \frac{n(\mathbf{r}', t)}{|\mathbf{r} - \mathbf{r}'|}. \quad (2.26)$$

Since the external potential is defined by the system under study and the Hartree potential only depends on the instantaneous density, the exchange-correlation potential must formally depend on the density at all previous times, the initial many-body wave function and the initial KS wave functions

$$v_{\text{xc}}(\mathbf{r}, t) = v_{\text{xc}} \left[n, \Psi_0, \left\{ \phi_i^{(0)} \right\}_{i=1}^N \right] (\mathbf{r}, t). \quad (2.27)$$

Making the assumption that the system initially is at rest, Ψ_0 must be the ground state many-body wave function which formally is a functional of the ground state density. The initial KS wave functions are the ground state KS wave functions. Thus the dependence on Ψ_0 and $\phi_i^{(0)}$ vanishes. Still, the *xc*-functional remains a complicated object that is difficult to describe.

2.3.2 Adiabatic approximation

The *adiabatic* approximation is commonly made, where a DFT *xc*-functional evaluated at the instantaneous density is taken as the the TDDFT *xc*-functional. The adiabatic *xc*-functional has no explicit time dependence or memory. It is exact when the external potential varies infinitely slowly (causing the system to always be in its ground state).

It has been shown that TDDFT with adiabatic *xc*-functionals predicts absorption spectra of metallic particles that are consistent with experimental data^{32,33}. This motivates the use of the adiabatic approximation throughout this thesis.

2.3.3 Photoabsorption in the linear response regime

In this thesis the photoabsorption spectrum is a major quantity of interest. It is a linear spectroscopic quantity, which is why we assume that the response of observables is linear in the time-dependent potential $v_1(\mathbf{r}, t)$. This requires $v_1(\mathbf{r}, t)$ to be weak enough to only slightly perturb the system. The linearity simplifies analysis as each frequency component of observables depends only on the corresponding frequency component of the perturbing potential. This section discusses the observables of interest in the thesis.

The induced density

$$\delta n(\mathbf{r}, t) = n(\mathbf{r}, t) - n(\mathbf{r}, 0) \quad (2.28)$$

shows how the system deviates from its equilibrium. Tracing it in time can be of interest in the study of ultra-fast excitations. Its Fourier transform $n(\mathbf{r}, \omega)$ is related to the strength of the response at a given frequency, *i.e.* the absorption spectrum. The induced dipole moment in a direction, *e.g.* x , is

$$\delta\mu^x(t) = - \int d\mathbf{r} x \delta n(\mathbf{r}, t). \quad (2.29)$$

The polarizability α_{ij} relates the induced dipole moment to the electric field strength in two not necessarily same directions i and j . For example, assuming the time-dependent potential has the form

$$v_1(\mathbf{r}, t) = z\mathcal{E}_z(t) \quad (2.30)$$

the induced dipole moment in x is

$$\delta\mu_x(t) = \int_{-\infty}^{\infty} \alpha_{xz}(t-t')\mathcal{E}_z(t') dt'. \quad (2.31)$$

The Fourier transform of the convolution on the right hand side is a product, allowing to write the Fourier transform of the polarizability

$$\alpha_{xz}(\omega) = \frac{\delta\mu^x(\omega)}{\mathcal{E}_z(\omega)}. \quad (2.32)$$

The imaginary part of the polarizability diagonal elements gives the oscillator strength function

$$S^z(\omega) = \frac{2\omega}{\pi} \text{Im}[\alpha_{zz}], \quad (2.33)$$

which equals to the optical absorption cross-section save for a constant pre-factor. Thus we can view $S^z(\omega)$ as the photoabsorption spectrum in the units of oscillator strength.

In general, the oscillator strength f_I is a measure of the strength of the optical excitation from the many-body ground state Ψ_0 with energy E_0 to an excited state Ψ_I with energy E_I . The discrete oscillator strength is linked to the continuous oscillator strength function $S(\omega)$ by

$$S(\omega) = \sum_I f_I \delta(\omega - (E_I - E_0)), \quad (2.34)$$

where δ is the Dirac delta function. Note however that we have only included (2.34) and the discussion of discrete oscillator strength for general context. In the explicit time propagation scheme employed in this thesis the discrete oscillator strengths are never directly computed.

The oscillator strengths satisfy the sum rule that they sum to the number of valence electrons

$$\sum_I f_I = N. \quad (2.35)$$

Because each delta function integrates to 1 the integral of the oscillator strength function must also be the number of electrons

$$\int_0^\infty S(\omega) d\omega = N. \quad (2.36)$$

3

(TD)DFT in practice

In this chapter the application of DFT and TDDFT is exemplified. The chapter contains a step-by-step description of calculations for an example system and introduces the reader to the electronic structure and plasmonic response of metal particles. In the ground state DFT calculations, a self-consistent algorithm for finding the KS orbitals is employed. Functions in space are represented numerically with either a finite difference method or in the efficient LCAO basis. Also the PAW method, density mixing and occupation number smearing are briefly introduced.

In the TDDFT calculations, an explicit time propagation scheme is utilized. An initial δ -kick perturbation is applied to the system, and the density response as a function of time is solved for. The δ -kick contains equal parts of all frequency components. As it is assumed that it is weak enough to only induce a linear response, the photoabsorption spectrum can be extracted. Also responses of observables to any general perturbation that has the same polarization direction as the δ -kick can be extracted.

The example system consists of eight atoms in a chain, illustrated in figure 3.1. The calculations are first done for a sodium (Na) atom chain to show the free-electron-gas-like behavior of the valence electrons. As silver is relevant for the remainder of the thesis, the calculations are repeated for a silver (Ag) atom chain. The calculations are done using the software GPAW^{17,34–38} and ASE³⁹.

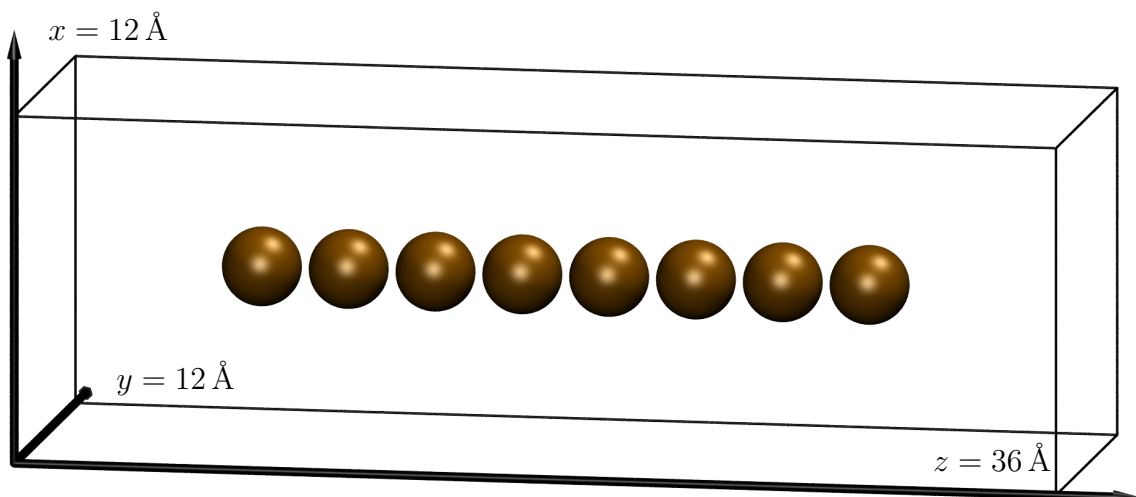


Figure 3.1: A linear chain of eight atoms, an example system considered throughout this chapter. The simulation box of $12 \text{ \AA} \times 12 \text{ \AA} \times 36 \text{ \AA}$ drawn.

3.1 Calculating the ground state with KS-DFT

The DFT calculation is set up by defining a simulation box of size $12 \text{ \AA} \times 12 \text{ \AA} \times 36 \text{ \AA}$ and the positions of 8 atoms in a chain. The atoms are placed in the middle of the box with 3 \AA between each neighbor. In such a way there is 6 \AA of vacuum between each atom and the closest edge of the box. The box and atoms are shown in figure 3.1.

The effective potential $v_{\text{eff}}[n](\mathbf{r})$, electronic density $n(\mathbf{r})$ and KS orbitals $\phi_i(\mathbf{r})$ are represented numerically in one of several possible ways. One such numerical representation is the *finite difference* method, where the functions are sampled on a grid in the simulation box, with a fixed distance between each grid point. Another representation is the LCAO method which is introduced in section 3.1.4. As boundary conditions, $v_{\text{eff}}[n](\mathbf{r})$ and $n(\mathbf{r})$ are set to zero at the edges of the box. A sufficiently large *vacuum size* (here 6 \AA) is needed between the atoms and the closest box edges to describe $v_{\text{eff}}[n](\mathbf{r})$ and $n(\mathbf{r})$ correctly.

Within the Born-Oppenheimer approximation the atomic nuclei are treated as fixed objects that define an external potential $v_{\text{ext}}(\mathbf{r})$ (2.15). Because the KS wave functions vary rapidly in the vicinity of the nuclei they would require a large computational effort to represent numerically. To circumvent this problem the projector augmented-wave (PAW) method⁴⁰ is used in GPAW. It defines a projection that maps the rapidly varying KS wave functions to smooth pseudo KS wave functions. The projection also takes into account the behavior of core electrons within the *frozen core* approximation, meaning that the core electrons are kept as for an isolated atom. By including only valence electrons the runtime of calculations is decreased. The PAW projector is unity outside a small region around each atom. Thus the pseudo KS wave functions and KS wave functions are equal everywhere except for near the nuclei.

The density is constructed from the N KS states to (2.13) corresponding to the lowest energies ε_i . Assuming the system is not spin polarized we can consider the spin indirectly by occupying every KS state twice. If N is even the ground state density is (if N is odd then the last term lacks the factor 2)

$$n(\mathbf{r}) = 2 \sum_{i=1}^{N/2} |\phi_i(\mathbf{r})|^2. \quad (3.1)$$

For molecular systems the highest occupied molecular orbital (HOMO) and lowest unoccupied molecular orbital (LUMO) are of special relevance. In Na_8 $\phi_4(\mathbf{r})$ is the HOMO and $\phi_5(\mathbf{r})$ the LUMO. We define the Fermi level μ to be any energy between the HOMO and LUMO energy. The precise energy of the Fermi level is specified later in the chapter when occupation number smearing is introduced. Thus all states below the Fermi level are occupied and all above are unoccupied.

A defining feature of bulk metallic systems is that both HOMO and LUMO are at the Fermi level. In finite metallic systems there is a small gap due to the discreteness of energy levels.

3.1.1 The self-consistent algorithm

The procedure for finding the KS orbitals is a self-consistent algorithm, summarized as a flowchart in figure 3.2. A trial electron density $n^{\text{trial}}(\mathbf{r})$ is guessed. The effective potential is constructed from equations (2.14) through (2.18). The KS equation (2.13) is solved for the $N/2$ lowest eigenvalues, which correspond to the occupied KS orbitals. The electronic density $n(\mathbf{r})$ is constructed according to equation (3.1). If the density $n(\mathbf{r})$ differs from the trial density $n^{\text{trial}}(\mathbf{r})$ by more than a small threshold, a new trial density $n^{\text{trial}}(\mathbf{r})$ is constructed according to a mixing scheme such as the Pulay⁴¹ mixing scheme, and the steps are repeated. When the change in the density $n(\mathbf{r})$, KS wave functions $\phi_i(\mathbf{r})$ and the total energy $E[n]$ between two iterations of the algorithm is smaller than a threshold, self-consistency is said to have been reached and the DFT calculation is done.

The mixing scheme could in the most simple case be to letting the output density be the trial density. In practice this often leads to the algorithm taking too large steps and getting stuck. The Pulay scheme suggests to let the trial density be a linear combination of the output density, and previous trial densities.

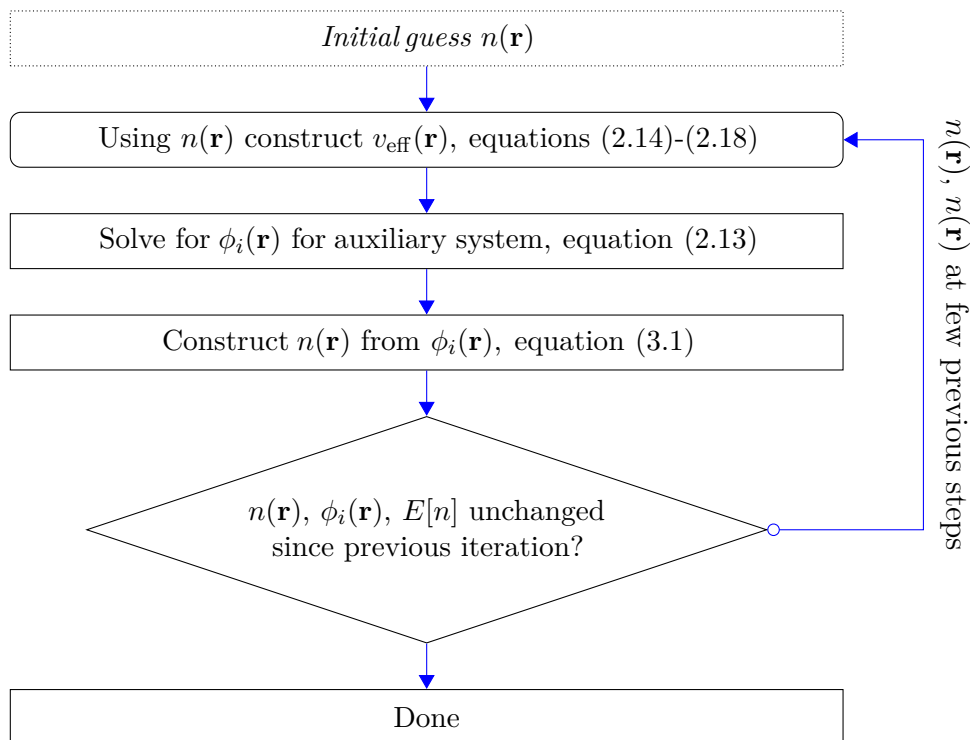


Figure 3.2: Self-consistent algorithm for finding the ground state density, described in section 3.1.1

3.1.2 Occupation number smearing

Within the scope of this thesis KS-DFT is a zero-temperature theory that dictates that the density should consist of the lowest KS orbitals. However the self-consistent algorithm may often converge slowly or not at all when following this rule. Instead a finite smearing parameter w may be introduced, defining a possibly fractional occupation number f_i . In GPAW, the density is constructed as

$$n(\mathbf{r}) = \sum_{i=1}^{\infty} f_i |\phi_i(\mathbf{r})|^2 \quad (3.2)$$

$$f_i = \frac{1}{1 + \exp[(\varepsilon_i - \mu)/w]}. \quad (3.3)$$

The occupation number has the same form as the Fermi-Dirac distribution which describes the distribution of states at finite temperatures. Its purpose is to approximate the step function and there are other viable smearing schemes which also can approximate it. It does not represent a true temperature effect.

3.1.3 Density of states

The density of states (DOS) is commonly used as a measure of the number of states at a certain energy (often per volume of the system). Within this thesis the DOS is a tool to visualize discrete KS energy levels ε_i as a continuous function. We define it

$$D(\varepsilon) = \sum_{i=1}^{\infty} g_i(\varepsilon) \quad (3.4)$$

where $g_i(\varepsilon)$ is a Gaussian function with an arbitrary broadening parameter σ

$$g_i(\varepsilon) = \frac{1}{\sqrt{2\pi\sigma^2}} \exp\left(-\frac{(\varepsilon_i - \varepsilon)^2}{2\sigma^2}\right). \quad (3.5)$$

The DOS has units of inverse energy. Integrating it over a range of energies yields the number of electrons in that energy range. In this chapter the broadening parameter $\sigma = 0.1$ eV is used.

3.1.4 The LCAO basis set

Expansion in a *linear combination of atomic orbitals* (LCAO) basis set is a more efficient numerical representation of spatial functions than the finite difference method. The LCAO basis set consists of a total of N_{basis} basis functions $\chi_{\mu}(\mathbf{r})$. Each $\chi_{\mu}(\mathbf{r})$ is centered around one of the atoms. The indexes μ can be arranged so that the first n_{basis} correspond to atom number 1, the next n_{basis} to atom number 2 and so on. However, in general the number of basis functions n_{basis} does not need to be the same for all atoms. The KS wave functions are written in the LCAO basis

$$\phi_i(\mathbf{r}) = \sum_{\mu=1}^{N_{\text{basis}}} C_{\mu i} \chi_{\mu}(\mathbf{r}), \quad (3.6)$$

where $C_{\mu i}$ is the LCAO coefficient for basis function μ of KS state i .

In GPAW, basis functions consist of numerical radial functions multiplied by spherical harmonics, and are typically generated to approximate the KS orbitals of isolated atoms. In this thesis the *double- ζ* polarized³⁷ (dzp) basis is used for predicting ground state properties. It includes two radial basis functions to describe each valence state of the isolated atoms, and a polarization function with the spherical harmonics corresponding to the first unoccupied state. A modified basis set¹⁷ is used to predict excited state properties, where the polarization function has been replaced with two radial functions approximating the lowest unoccupied KS state of the isolated atom.

The advantage of LCAO over the finite difference method can be illustrated by considering the number of parameters needed to represent spatial functions. With a simulation box of size $12 \text{ \AA} \times 12 \text{ \AA} \times 36 \text{ \AA}$ with 0.3 \AA between grid points 192 000 points are required in finite difference mode. The aforementioned modified basis sets have 8 basis functions per atom for Na and 18 for Ag respectively. With 8 atoms the number of LCAO coefficients $C_{\mu i}$ needed is $8 \times 8 = 64$ for Na and $8 \times 18 = 144$ for Ag. Contrasting this to the 192 000 points needed in the finite difference mode shows why it is advantageous to use LCAO for larger systems.

3.1.5 Ground state properties of Na and Ag chains

Figure 3.3 shows a selection of the converged KS orbitals and corresponding energies for Na_8 with the LDA *xc*-functional. In LCAO the KS orbitals are represented by the LCAO expansion, and the density and potential are calculated on a grid with 0.3 \AA between grid points. In finite difference mode the KS orbitals, density and potential are represented on a grid, with a tighter grid spacing of 0.09375 \AA . The energies are measured relative to the potential at the edges of the box, which is called the vacuum level. States below the vacuum level are localized to the vicinity of the atoms. The difference between occupied states calculated with the finite difference and LCAO methods is small, justifying the use of the cheaper LCAO method.

The orbitals are ordered in energy according to the number of nodes in the density, which is expected of a 1-dimensional electron gas. This is clearly seen for states below -1.5 eV with respect to vacuum level. At -1.5 eV another sequence of orbitals begins, with one node perpendicular to the chain axis. These states are always degenerate because of the two symmetrically equivalent directions.

Above vacuum level the states are expected to be plane wave-like with the density evenly distributed in space. In reality there should be a continuum of states but this cannot be captured by the finite size simulation box. There are large differences between the LCAO and finite difference methods, because LCAO lacks the degrees of freedom to describe the plane wave-like states.

Figure 3.4 shows the densities of state for Na_8 and Ag_8 with the LDA and GLLB-SC *xc*-functionals. Note that energies are shown with respect to Fermi level. The Ag atom has 1 s-type and 10 d-type valence electrons, while Na has just one s-type electron. Between -1 eV and 1 eV the DOS of Ag is similar to the DOS of Na. This part of the DOS comes from the s-electrons. Below -2 eV in Ag there is a large peak, which comes from the d-electrons.

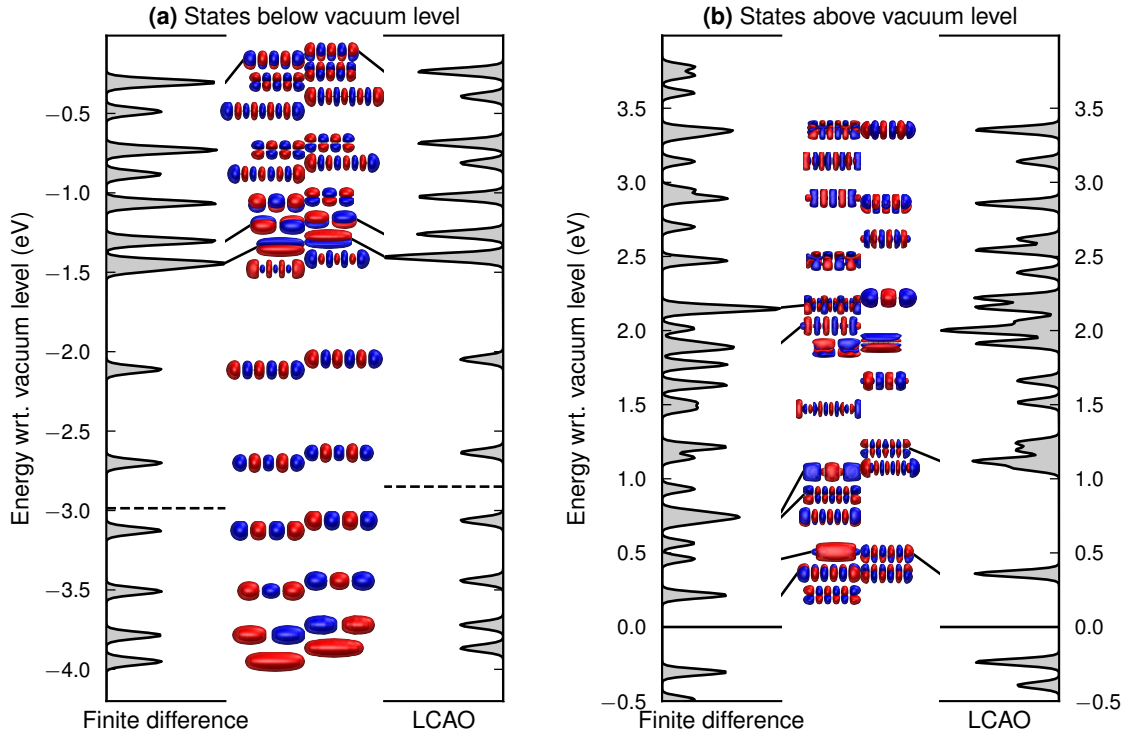


Figure 3.3: Densities of state and isosurfaces of selected KS orbitals for Na_8 in finite difference and LCAO mode. The Fermi level with finite difference/LCAO is marked with dashed lines. Isosurfaces of states are drawn at the corresponding energies (in the case of nearby states a line points to the correct energy). Degenerate states show up as larger peaks in the DOS.

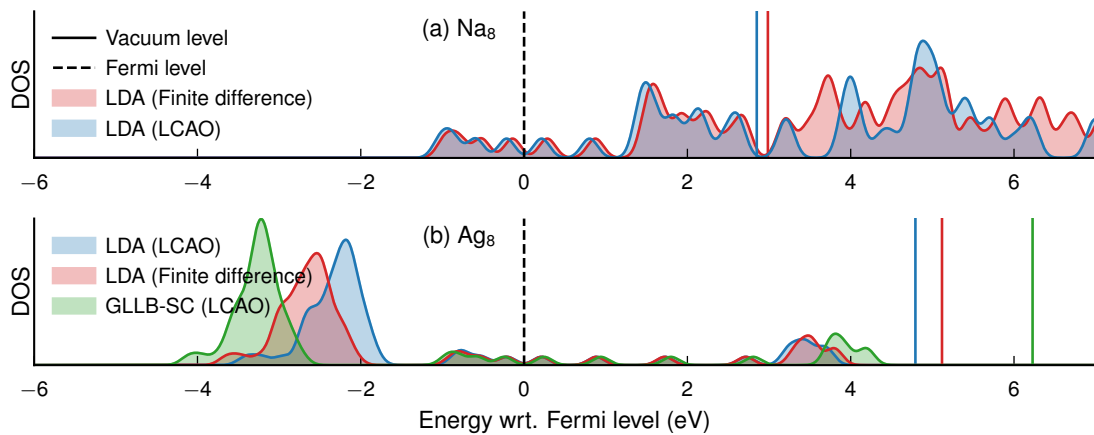


Figure 3.4: Densities of states for Na and Ag chains with finite difference/LCAO mode and LDA/GLLB-SC functional.

The position of the d-electron peak in Ag depends on the xc -functional choice and whether finite difference or LCAO is used. The shift to lower energies in GLLB-SC is a desired feature of the functional^{17,29,30}. The difference between LCAO and the finite difference method indicates that the present basis set is insufficient in describing Ag atom chains, as these ideally should not differ. For NPs which are of real interest in this thesis the present basis set has been shown to give the correct DOS¹⁷.

3.2 Calculating optical properties with TDDFT

The optical properties of the example system can be calculated from the response of the time-dependent KS orbitals $\phi_i(\mathbf{r}, t)$ to some time-dependent external potential $v_{\text{ext}}(\mathbf{r}, t)$. In this thesis an explicit time propagation scheme with a δ -kick is employed, where the external potential is

$$v_{\text{kick}}(\mathbf{r}, t) = \mathcal{E}z\delta(t). \quad (3.7)$$

As we are interested in the optical properties in the chain axis direction, the field is polarized in the z direction. However for a full description of the optical properties of non-isotropic systems up to three separate time propagation calculations with differently polarized kicks are needed. This is seen in chapter 4.

The kick-strength is set to $\mathcal{E} = 1 \times 10^{-5} \text{ eV \AA}^{-1}$ which is assumed to be weak enough for the non-linear response to be negligible. The linearity of the response allows us to extract the photoabsorption spectrum (in the polarization direction) and the response to any other perturbation with the same polarization from the response to the δ -kick. Relevant other perturbations are monochromatic laser fields, and ultra-short laser pulses.

As the NPs in this thesis are much smaller than the wavelength of visible light, we can consider the electric field as constant in space but varying in time. In this so called *dipole approximation*, the potential of an monochromatic laser field polarized in the z direction has the form

$$v_{\text{laser}}(\mathbf{r}, t) = \mathcal{E}z \sin(\omega t). \quad (3.8)$$

The ultra-short laser pulse used in chapter 5 is centered around time t_0 and has a parameter τ that determines its duration

$$v_{\text{ultra-short-pulse}}(\mathbf{r}, t) = \mathcal{E}z \sin(\omega t) \exp\left(-\frac{(t-t_0)^2}{\tau^2}\right). \quad (3.9)$$

The three relevant potentials $v_{\text{laser}}(\mathbf{r}, t)$, $v_{\text{ultra-short-pulse}}(\mathbf{r}, t)$ and $v_{\text{kick}}(\mathbf{r}, t)$ are shown in the time- and frequency domains in figure 3.5 at some value \mathbf{r} . The spatial dependence is not shown as all potentials are proportional to z . Because the Fourier transform of the δ -kick contains all frequencies (with equal proportions), responses to the other perturbations can be extracted from the response to the δ -kick.

The time-dependent KS equation (2.24) is a differential equation with the initial condition that the KS orbitals are the ground state KS orbitals $\phi_i(\mathbf{r}, 0) =$

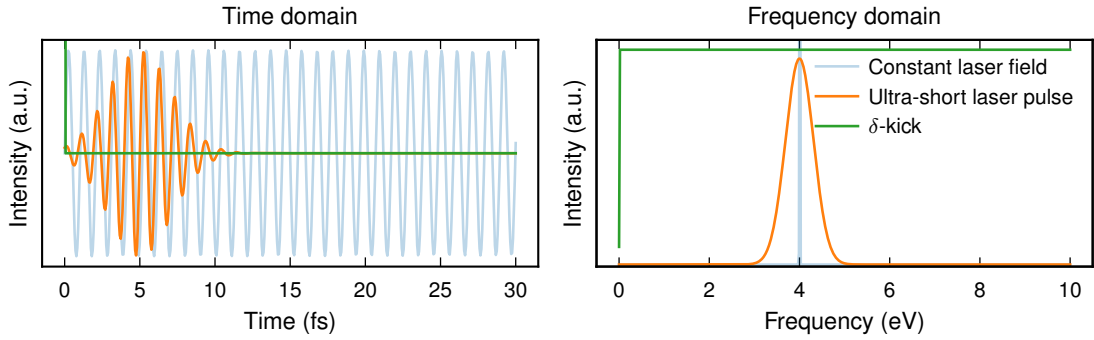


Figure 3.5: Relevant external potentials in the time and frequency domains. The three potentials v_{laser} , $v_{\text{ultra-short-pulse}}$ and v_{kick} are evaluated at some point \mathbf{r} . In the linear-response regime the response to any pulse can be recovered from the response to the δ -kick, which contains equal amounts of all frequencies.

$\phi^{(0)}(\mathbf{r})$. Letting the external potential be the δ -kick the time-dependent KS orbitals are calculated at subsequent points in time with the Crank-Nicholson algorithm which is suitable for solving differential equations implicit in time. In this chapter the size of the time steps is 20 as and the total length of the propagation 30 fs.

3.2.1 Calculating observables

Some observables, such as the dipole moment or induced density from the δ -kick, are obtained directly in the calculations. For example by recording the dipole moment for all time steps during the propagation, and taking its Fourier transform the photoabsorption spectrum can be obtained. To obtain responses to other perturbations than the δ -kick, we express the observables in terms of the KS density matrix operator.

The KS density matrix operator is defined

$$\hat{\rho}(t) = \sum_n |\phi_n(t)\rangle f_n \langle \phi_n(t)|, \quad (3.10)$$

where f_n is the occupation number of state n . It is written in the basis of ground state KS orbitals

$$\rho_{ia}(t) = \langle \phi_i^{(0)} | \hat{\rho}(t) | \phi_a^{(0)} \rangle = \sum_m \int d\mathbf{r} d\mathbf{r}' f_m \phi_i^{(0)*}(\mathbf{r}) \phi_m(\mathbf{r}, t) \phi_m^*(\mathbf{r}', t) \phi_a^{(0)}(\mathbf{r}'), \quad (3.11)$$

where i and a are occupied and unoccupied KS states respectively. From the KS density matrix of the δ -kick $\rho_{ia}^{\text{kick}}(t)$ of strength \mathcal{E}_0 , the KS density matrix of any other perturbation $v_{\text{ext}}(t)$ can be obtained as a convolution

$$\rho_{ia}(t) = \frac{1}{\mathcal{E}_0} \int d\tau \rho_{ia}^{\text{kick}}(\tau) v_{\text{ext}}(t - \tau). \quad (3.12)$$

Equivalently in frequency space

$$\rho_{ia}(\omega) = \frac{1}{\mathcal{E}_0} \rho_{ia}^{\text{kick}}(\omega) v_{\text{ext}}(\omega). \quad (3.13)$$

During time propagation, each matrix element $\rho_{ia}^{\text{kick}}(t)$ of the δ -kick KS density matrix at each time step is saved.

From the real part of the induced KS density matrix elements

$$\text{Re } \delta\rho_{ia}(t) = \text{Re} [\rho_{ia}(t) - \rho_{ia}(0)] \quad (3.14)$$

the induced density is obtained

$$\delta n(\mathbf{r}, t) = 2 \sum_{ia}^{f_i > f_a} \phi_i^{(0)}(\mathbf{r}) \phi_a^{(0)*}(\mathbf{r}) \text{Re } \delta\rho_{ia}(t). \quad (3.15)$$

The induced dipole moment in the x direction is

$$\begin{aligned} \delta\mu^x(t) &= - \int d\mathbf{r} x \delta n(\mathbf{r}, t) \\ &= -2 \int d\mathbf{r} x \sum_{ia}^{f_i < f_a} \phi_i^{(0)}(\mathbf{r}) \phi_a^{(0)*}(\mathbf{r}) \text{Re } \delta\rho_{ia}(t) \\ &= -2 \sum_{ia}^{f_i < f_a} \mu_{ia}^x \text{Re } \delta\rho_{ia}(t) \end{aligned} \quad (3.16)$$

where the dipole matrix elements in the x direction are

$$\mu_{ia}^x = \int d\mathbf{r} x \phi_i^{(0)*}(\mathbf{r}) \phi_a^{(0)}(\mathbf{r}). \quad (3.17)$$

An important reminder to the reader concerning Fourier transforms is that the real part of a Fourier transform of a function is not in general the same as the Fourier transform of the real part of the function. In the following the Fourier transform of the real part of the induced KS density matrix is denoted $[\text{Re } \delta\rho_{ia}](\omega)$. Writing the induced dipole moment as a convolution of the polarizability

$$\int_{-\infty}^{\infty} \alpha_{xz}(t - t') \mathcal{E}_z(t') dt' = -2 \sum_{ia}^{f_i < f_a} \mu_{ia}^x \text{Re } \delta\rho_{ia}(t). \quad (3.18)$$

and taking the Fourier transform

$$\alpha_{xz}(\omega) = -\frac{1}{\mathcal{E}_z(\omega)} 2 \sum_{ia}^{f_i < f_a} \mu_{ia}^x [\text{Re } \delta\rho_{ia}](\omega) \quad (3.19)$$

gives the polarizability. Its imaginary part gives the photoabsorption spectrum. To summarize, the photoabsorption spectrum and induced density in terms of the KS density matrix are

$$S(\omega) = -\frac{1}{\mathcal{E}_z(\omega)} \frac{4\omega}{\pi} \sum_{ia} \text{Im}[\mu_{ia}^z [\text{Re } \delta\rho_{ia}](\omega)] \quad (3.20)$$

$$\delta n(\mathbf{r}, \omega) = 2 \sum_{ia} \phi_i^{(0)}(\mathbf{r}) \phi_a^{(0)*}(\mathbf{r}) [\text{Re } \delta\rho_{ia}](\omega). \quad (3.21)$$

Since the photoabsorption spectrum (3.20) and induced density (3.21) are both sums over all possible occupied-unoccupied pairs ia , the quantities can be divided into contributions from occupied-unoccupied state transitions.

$$S(\omega) = \sum_{ia} S_{ia}(\omega) \quad (3.22)$$

$$S_{ia}(\omega) = -\frac{1}{\mathcal{E}_z(\omega)} \frac{4\omega}{\pi} \text{Im}[\mu_{ia}^z * [\text{Re } \delta\rho_{ia}](\omega)] \quad (3.23)$$

$$\delta n(\mathbf{r}, \omega) = \sum_{ia} \delta n_{ia}(\mathbf{r}, \omega) \quad (3.24)$$

$$\delta n_{ia}(\mathbf{r}, \omega) = 2\phi_i^{(0)}(\mathbf{r})\phi_a^{(0)*}(\mathbf{r})[\text{Re } \delta\rho_{ia}](\omega). \quad (3.25)$$

A visual representation of $S_{ia}(\omega)$ can be obtained by constructing a *transition contribution map* (TCM) for a given frequency

$$M(\omega, \varepsilon_o, \varepsilon_u) = \sum_{ia} \frac{S_{ia}(\omega)}{S(\omega)} g_i(\varepsilon_o) g_a(\varepsilon_u) \quad (3.26)$$

$$g_i(\varepsilon) = \frac{1}{\sqrt{2\pi\sigma^2}} \exp\left(-\frac{(\varepsilon_i - \varepsilon)^2}{2\sigma^2}\right). \quad (3.27)$$

The broadening parameter in this chapter is 0.1 eV.

3.2.2 Optical properties of Na and Ag chains

The photoabsorption spectra for Na_8 and Ag_8 are shown in figure 3.6. Both systems have a distinct LSPR peak near 1 eV in the spectrum. For Ag the LSPR peak position increases when replacing the LDA xc -functional with GLLB-SC, as the position of the d-electron peak in the DOS changes.

Figure 3.7 shows the TCMs at the LSPR frequency of each system. The main contribution to the absorption peak is a transition from the KS state just below the Fermi level to the state just above it. Ag_8 additionally has negative contributions to the absorption which are transitions from the d-band to unoccupied levels.

The TCMs of Na_8 and Ag_8 with LDA at the LSPR are shown together with induced densities in figure 3.8. For Ag_8 the main positive contribution, and a few of the negative contributions, are shown separately (together with corresponding induced density contributions $\delta n_{ia}(\mathbf{r}, \omega)$). While the total induced densities differ between Na_8 and Ag_8 (panels (a) vs. (b)) the constructive contributions are similar (panels (a) vs. (c)). The negative contributions in Ag_8 (panel (d)) screen the plasmon by being oriented in the opposite direction. Na_8 lacks the negative contributions because it doesn't have d-type electrons.

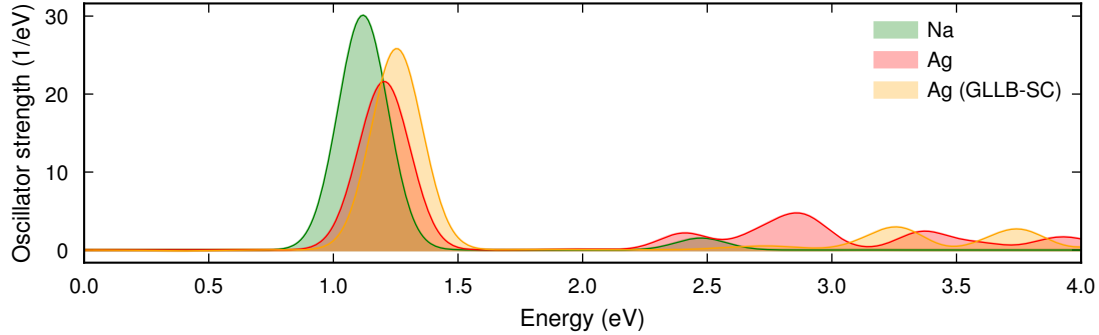


Figure 3.6: The photoabsorption spectrum in the chain axis direction for the Na_8 and Ag_8 atom chains. The legend marks the used xc -functional.

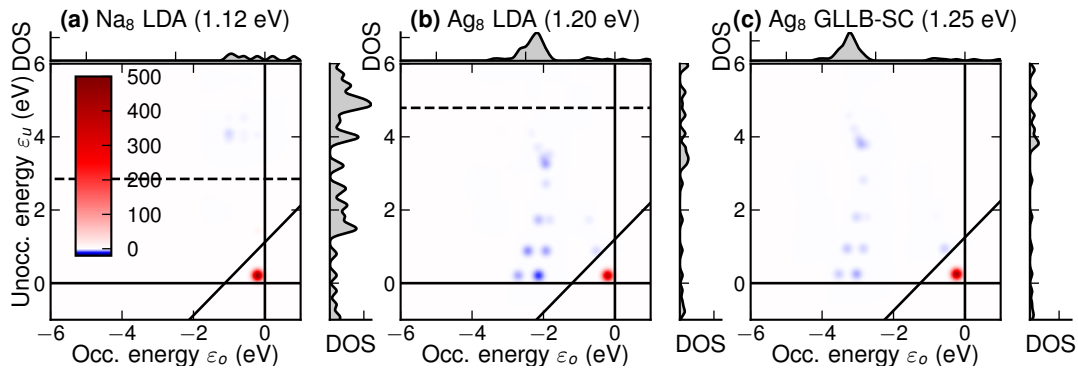


Figure 3.7: Transition contribution maps for Na_8 and Ag_8 . The TCM $M(\omega, \varepsilon_o, \varepsilon_u)$ at the LSPR is drawn as a heatmap. The densities of state corresponding to unoccupied and occupied states i and a are drawn along its edges. In each subpanel the LSPR frequency is given in paranthesis. This TCM is essentially a visualization of the matrix elements of $S_{ia}(\omega)$, meaning that positive values (red) correspond to states contributing to the photoabsorption and and negative values (blue) to damping the absorption. The units of the colorbar are eV^{-1} .

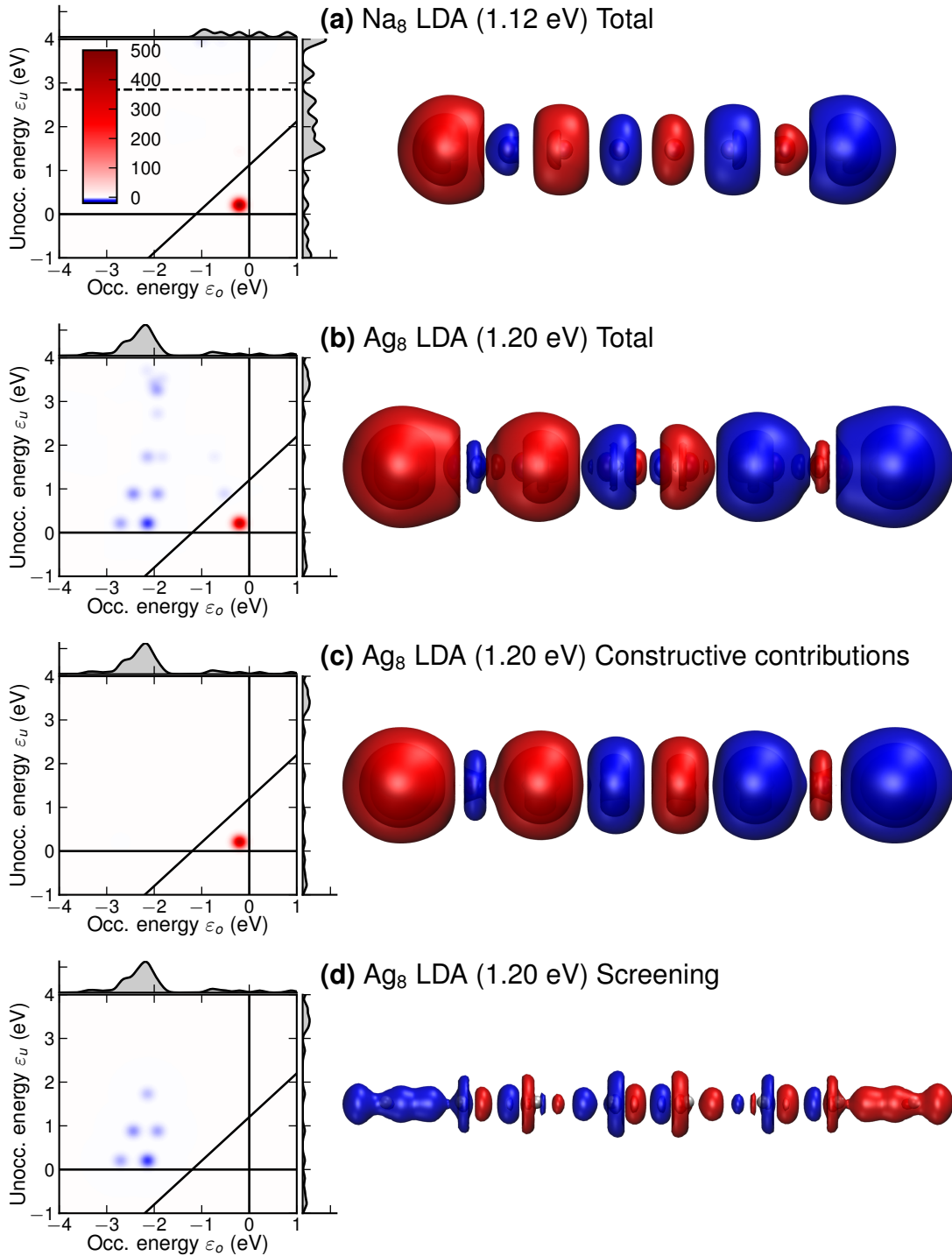


Figure 3.8: Isosurfaces of induced densities $\delta n(\mathbf{r}, \omega)$ at the LSPR. Each panel shows the induced density (to the right) from either all or a part of the transitions and the corresponding transitions marked in the TCM (to the left). (a) The Na₈ excitation, which consists of (nearly) one transition. (b) The Ag₈ excitation, which can be divided into constructive contributions (c) and screening (d). The units of the colorbar are eV⁻¹.

4

Size dependence of photoabsorption spectra

Experimentally fabricated NPs usually consist of a varying number of atoms. In any real measurement of NP ensembles, the optical properties will be an average of the properties of the individual NPs. Also the shape and substrate which the NPs are on will affect the optical properties, although that is beyond the scope of this thesis.

In this chapter the photoabsorption spectra for Ag NPs with shapes close to truncated octahedra (TO) are presented. The NPs consist of between 13 and 586 atoms. TO shapes are the lowest energy geometries for large NPs because they can be constructed by truncating a FCC lattice with $\{111\}$ and $\{100\}$ faces, without straining the structure. In the size range considered here other shapes (such as icosahedra) are more energetically favored, however their high strain can affect their optical properties and make analysis more difficult¹⁸.

Rahm and Erhart¹⁸ have determined the minimum energy geometry of TO-like NPs of all sizes considered here with Monte Carlo simulations in an embedded atom method (EAM) potential⁴². Starting with the Ag atoms in the positions determined by Rahm and Erhart¹⁸ the ground state is computed with the PBE *xc*-potential. Each atom is shifted by a small distance in the direction of the force acting on it and the ground state is computed again. This procedure, called a *relaxation* calculation, is repeated until the maximal force on an atom is 0.01 eV \AA^{-1} . For the spectrum calculations the ground state is computed with GLLB-SC from the relaxed PBE geometry and propagated through time for 30 fs with adiabatic GLLB-SC. The *dzp* LCAO basis set is used for the relaxation calculations, while a basis set optimized by Kuisma *et al.*¹⁷ to represent bound unoccupied states is used for the time propagation calculations.

Since every TDDFT calculation is fairly expensive in terms of computational resources the NPs are sampled rather sparsely. At the beginning of the chapter the chosen NPs are discussed. Then the energies of the structures are discussed and then the spectra. Finally it is shown that the spectra are converged with respect to the numerical parameters in the calculations.

4.1 Selected structures

Several NPs between 13 and 586 atoms in size have been selected for DFT and TDDFT investigation. A representative subset of them is pictured in figure 4.1. The Ag_{38} , Ag_{201} and Ag_{586} NPs are so called regular truncated octahedra (RTOs) with

8 identical and equilateral $\{111\}$ faces, truncated by $\{100\}$ faces. A few truncated octahedra, rugby-like and egg-like structures are also shown.

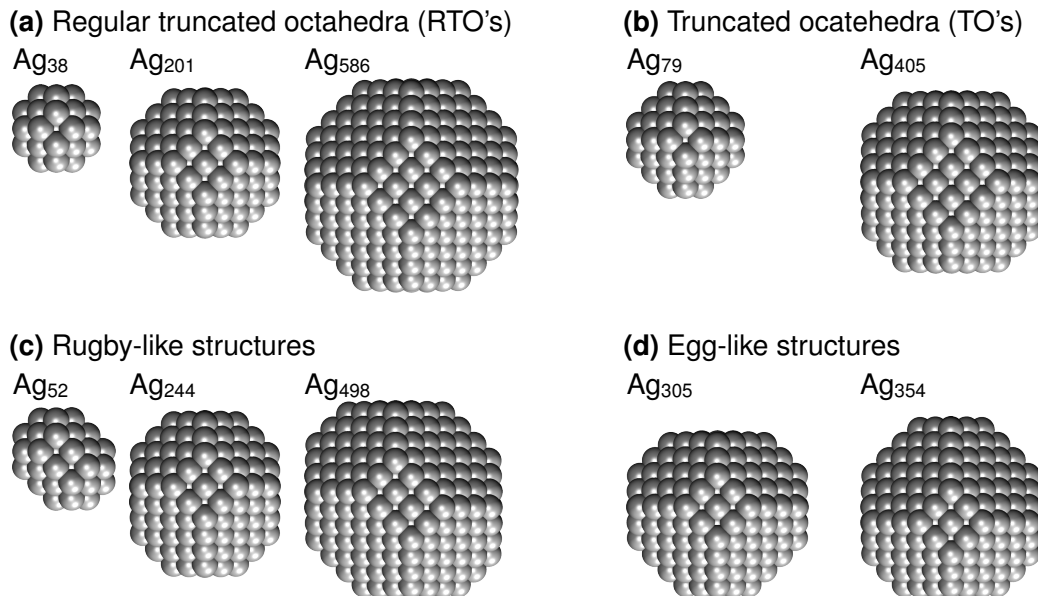


Figure 4.1: Classification of some of the NPs studied in this chapter. (a) The regular truncated octahedra (RTOs) Ag₃₈, Ag₂₀₁ and Ag₅₈₆ have 8 identical and equilateral $\{111\}$ faces, truncated by 6 $\{100\}$ faces. (b) The TOs Ag₇₉ and Ag₄₀₅ are similar but the $\{111\}$ faces are not equilateral. (c) The rugby-like and (d) egg-like structures resemble TOs that have been elongated both ways and one way respectively along some axis.

4.2 Size dependence of energies

The PBE ground state energies of the relaxed NPs are shown in figure 4.2 along with the EAM cohesive energies of Rahm and Erhart¹⁸. The latter per atom energies closely follow a third degree empirical polynomial in $N^{-1/3}$

$$\frac{E}{N} = a + bN^{-1/3} + cN^{-2/3} + dN^{-1}. \quad (4.1)$$

By directly comparing the per atom energies in figure 4.2 it is difficult to draw other conclusions than that they are decreasing with increasing NP size. Instead the energies are compared to a common fit. Fitting the EAM RTOs ($N = 38, 201, 586, 1289, 2406$) to equation (4.1) shows that all other TO-like geometries are higher in energy than the fit. The difference is up to 60 meV/atom for the smaller NPs and between 0 and 10 meV/atom for $N > 70$. The three first RTOs have been studied with DFT, so an exact fit to (4.1) to them can be made after setting $d = 0$. The differences between the PBE energies and the corresponding fit to RTOs are greater

in magnitude than with the EAM potential. Additionally two of the rugby-like structures (Ag_{52} and Ag_{244}) are lower in energy than the fit.

In contrast to the EAM potential which predicts the highest symmetry structures (RTOs) to be energetically most favorable, the PBE xc -functional with a dzp LCAO basis set favors small rugby-like structures more. This could implicate that they should be present in a larger fraction in manufactured NPs than EAM potentials predict.

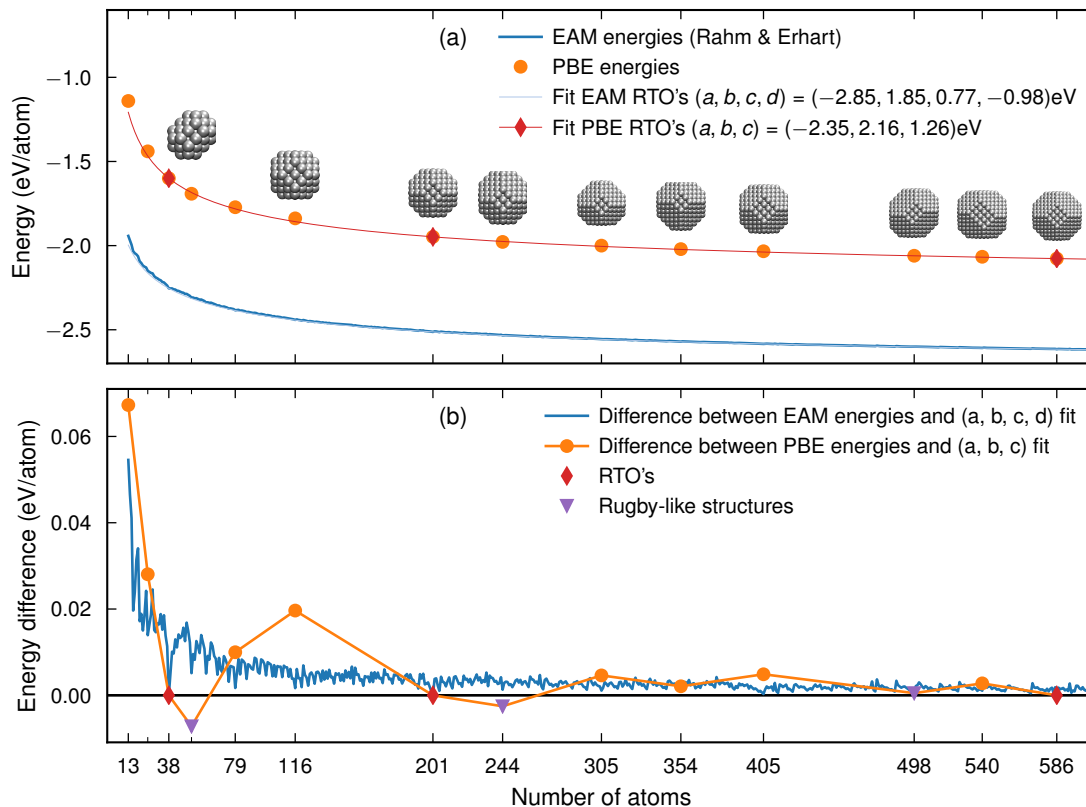


Figure 4.2: (a) Energies of NPs as calculated from an EAM potential and DFT calculations with the PBE xc -functional with a dzp LCAO basis set. The energies of RTOs are fitted to (4.1) (for EAM, data is available for sizes outside the range of the figure). (b) Difference between energies in (a) and the corresponding fits. In general non-RTOs energies are underestimated by the fit, but PBE Ag_{52} and Ag_{244} are exceptions to this.

4.3 Calculated spectra

The photoabsorption spectra for several selected NPs are shown in figure 4.3. Gaussian broadening with the parameter $\sigma = 0.1$ eV is used to present all spectra in this section. LSPR peaks are clearly visible in the spectra. The fully isotropic system Ag_{38} has identical spectra for all excitation directions, while Ag_{52} has the two equiva-

4. Size dependence of photoabsorption spectra

lent directions x and y , and Ag_{25} has three different spectra. There are clear LSPRs around 3.5–4 eV. Within one system, such as Ag_{52} , the LSPR peak frequencies in different excitation directions can differ by a few hundred meV. In certain systems, such as Ag_{116} , there are two distinct peaks, while for certain systems (*e.g.* Ag_{52} in x direction) two peaks are close enough to appear as one wide peak with the chosen value of the Gaussian broadening parameter.

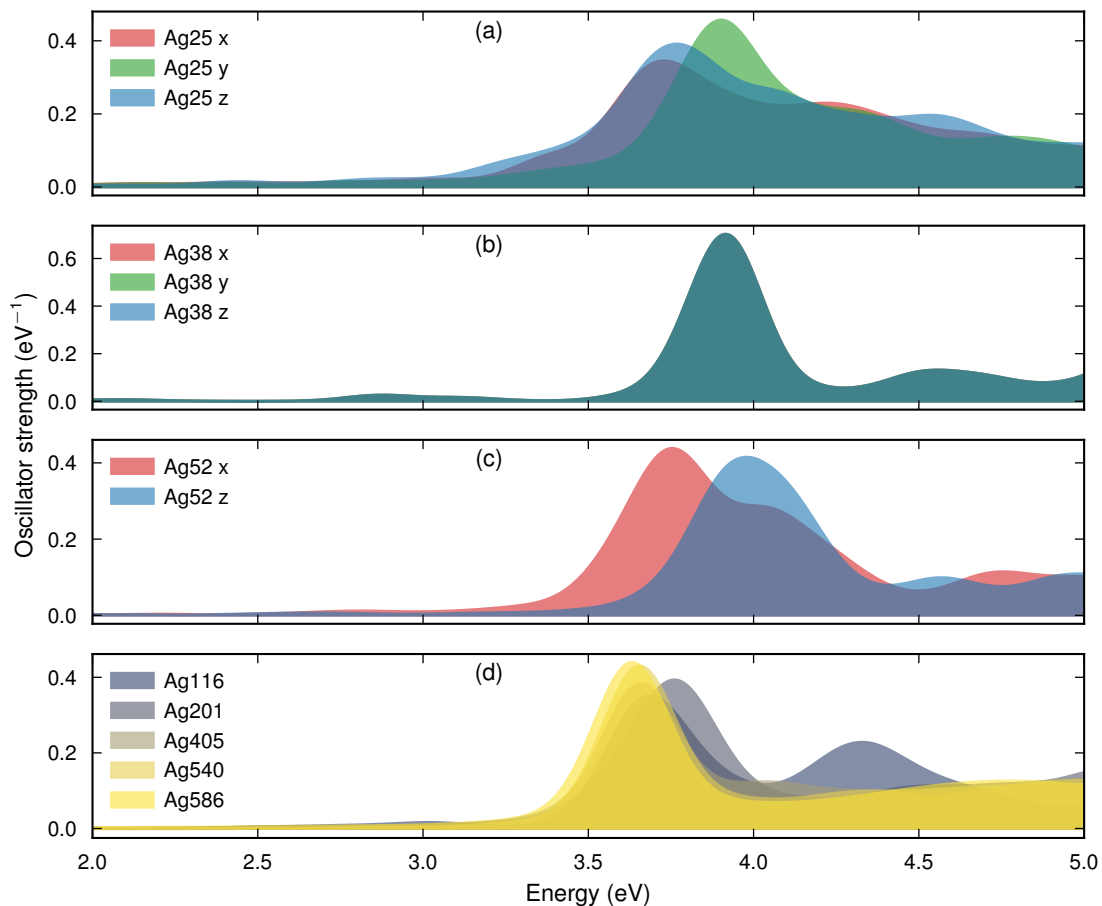


Figure 4.3: Photoabsorption spectra for selected NPs. For systems that are not isotropic the absorption spectra in two (*e.g.* Ag_{52}) or three (*e.g.* Ag_{25}) excitation directions have to be distinguished.

In an ensemble of NPs with no preferential alignment the measured spectra will be an average over the present sizes and all excitation directions. It is therefore meaningful to consider direction-averaged spectra for non-isotropic NPs. These are presented in figure 4.4. Extracted frequencies, widths at half maximum and intensities of the main LSPR peaks are shown in figure 4.5. In the large NP range ($N \geq 201$) there appears to be a linear dependence of the LSPR peak position versus $N^{-1/3}$. This is consistent with classical results with non-local dielectric functions for spherical NPs⁴³ which predict a dependence on the diameter D as $1/D$. A similar trend has also been observed for icosahedral Ag NPs in the same size range¹⁷.

Figure 4.5 shows a fit of the peak frequencies for $N \geq 201$ to a linear function in $N^{-1/3}$. In this size range, the peak frequencies are at most 2% off from the fit. In the large-size limit the fit extrapolates the peak frequency to 3.34 eV. This is fairly close to the peak energies obtained with quasi-static finite difference time-domain electromagnetic calculations with experimental Ag dielectric functions for icosahedral and spherical NPs, which are 3.43 eV and 3.52 eV respectively¹⁷.

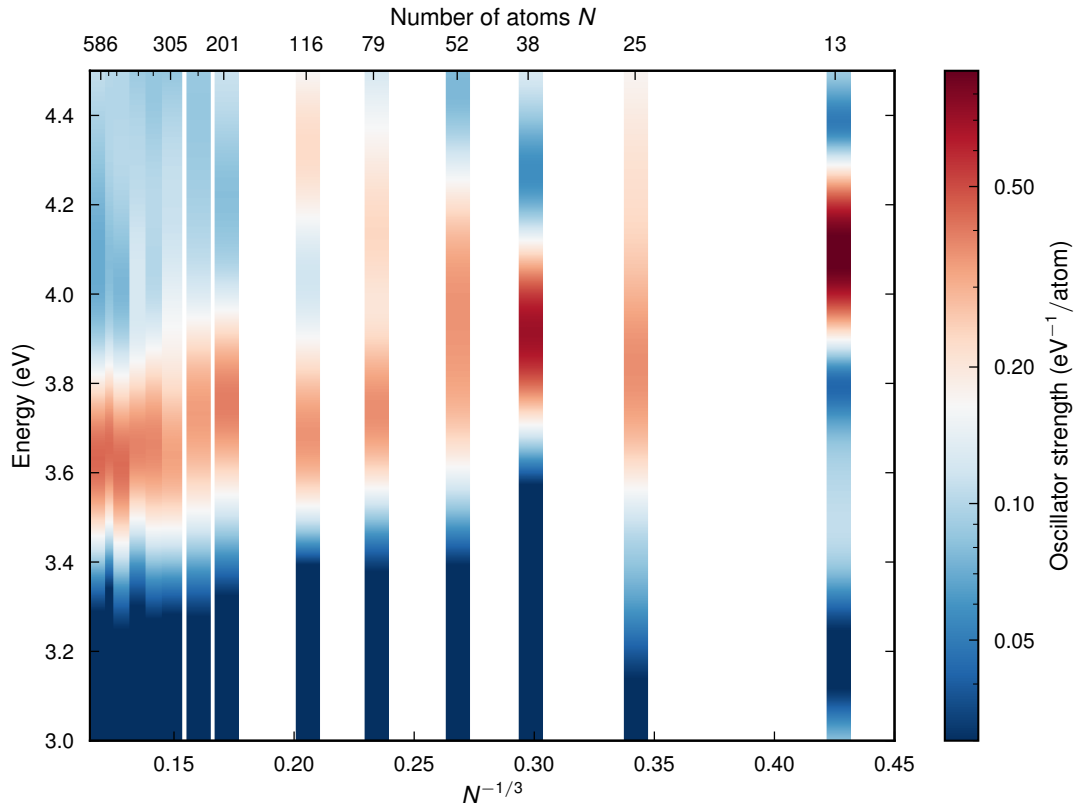


Figure 4.4: Direction averaged spectra of NPs as a function of $N^{-1/3}$. Above $N = 200$ the LSPR frequency appears to depend linearly on $N^{-1/3}$ with little variation in width or intensity. Smaller NPs follow a similar trend with more scatter in frequency, width and intensity. For Ag₅₂ through Ag₁₁₆ two peaks are visible.

4. Size dependence of photoabsorption spectra

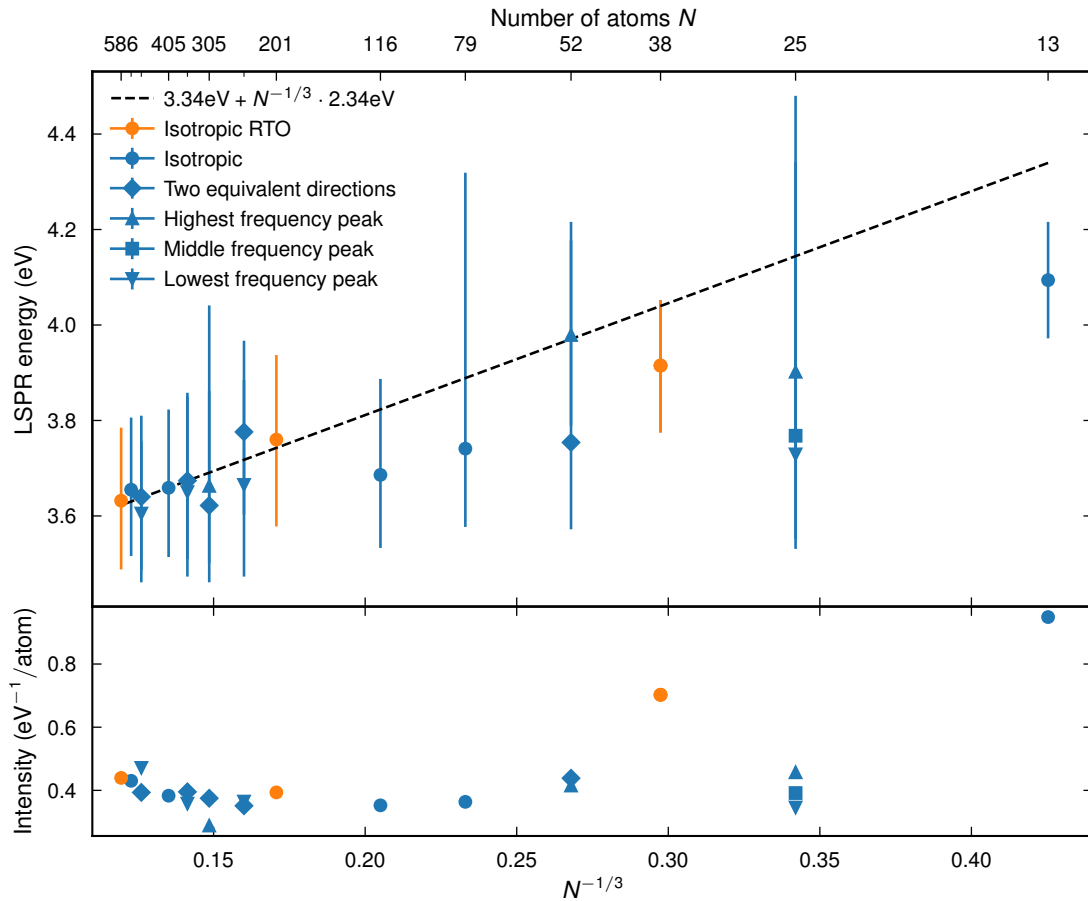


Figure 4.5: The LSPR energy (a) and intensity (b) versus $N^{-1/3}$. The bars indicate the width of the peaks at half maximum. The symbols and colors indicate if the NP is a RTO, a different isotropic structure, or a structure of lower symmetry, in which case the peaks in spectra in different excitation directions are shown. For $N \geq 201$ the LSPR peak frequencies have been fitted to a linear function in $N^{-1/3}$. In this size range there is little variation in peak width or intensity. Smaller NPs follow a similar trend with more scatter in frequency, width and intensity.

4.4 Choice of numerical parameters

In the DFT and TDDFT calculations there are parameters which should be extremized to get accurate results, but come with a computational cost. The following are most prominent:

- The extent of vacuum on each side of the NP. In principle this should be infinite to describe an isolated particle but it is sufficient and computationally reasonable to consider a few Ångström. This parameter is denoted v .
- The grid spacing used to represent the electron density of the system. In principle it should be infinitesimally small. It is denoted h .
- The time step taken during the time propagation. This parameter is denoted dt and should also be as small as possible.

For this thesis, the parameters $v = 6 \text{ \AA}$, $h = 0.3 \text{ \AA}$ and $dt = 10 \text{ as}$ have been chosen to be a good tradeoff between computational speed and accuracy based on a convergence test. The photoabsorption spectrum of the Ag_{13} cluster was calculated while keeping two of the parameters fixed and varying the third. The results are seen in figure 4.6. The appearance of the spectrum below 6 eV is practically unchanged for values of $v = 5 \text{ \AA}$ or more and $h = 0.3 \text{ \AA}$ or less. The decrease of dt seems to blueshift all peaks consistently, with some changes in intensity. It is not yet fully converged even at 5 as however 10 as is chosen to get reasonable computational times. For large energies 6 eV there is more variation in the spectrum with respect to the parameters. Such high energy contributions are disregarded, as they stem from unbound unoccupied states which are inadequately described with LCAO basis sets.

4. Size dependence of photoabsorption spectra

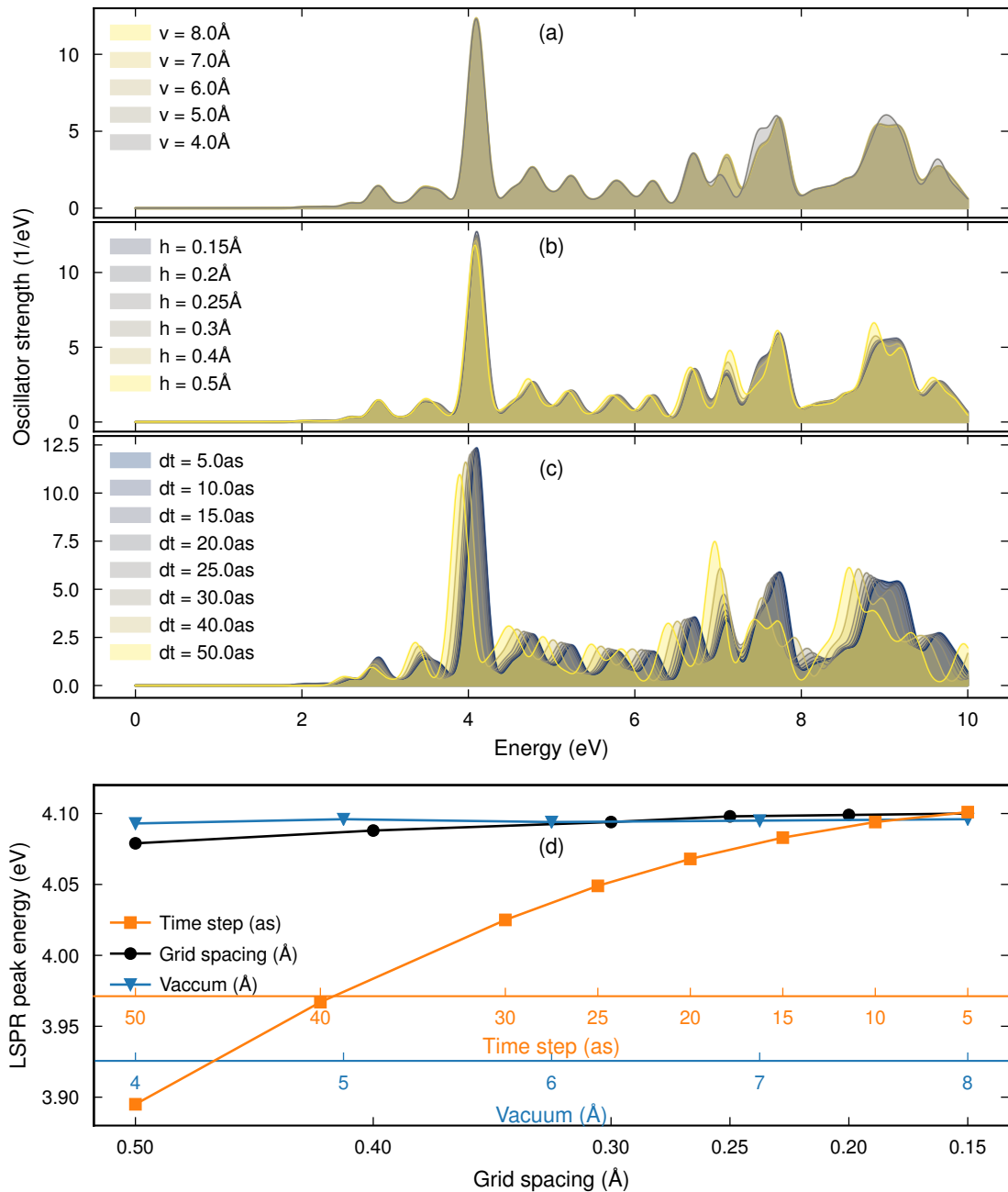


Figure 4.6: Convergence check for the parameters v , h and dt . Keeping two of the parameters fixed at $v = 6 \text{ \AA}$, $h = 0.3 \text{ \AA}$, $dt = 10 \text{ as}$ and varying the third the photoabsorption spectrum of Ag_{13} is calculated. **(a)** Varying v , **(b)** h and **(c)** dt . At energies below 6 eV the spectrum is barely affected when varying v but shows a blueshift of the peak with decreasing dt . **(d)** Summarizes the above by showing the LSPR peak energy versus each of the varied parameters. v and h are taken to be converged at the chosen values. The time step dt is not as clearly converged at 10 as however this value is chosen to keep computation times reasonably short.

4.5 Summary

- Truncated octahedron-like NPs consisting of between $N = 13$ and 586 atoms were studied
- The structures (obtained from a study using a EAM potential) were relaxed with the PBE *xc*-functional with a dzp LCAO basis set, obtaining ground state energies
 - Per atom energies were found to approximately follow a third degree polynomial in $N^{-1/3}$
 - The energies of regular truncated octahedra and small rugby-like structures were found to be lower than the trend
- Photoabsorption spectra were calculated with the GLLB-SC *xc*-functional and a LCAO basis set suitable to describe bound unoccupied states
 - The LSPR peak energy was found to be linear in $N^{-1/3}$ for $N \geq 201$, even for irregular shapes

4. Size dependence of photoabsorption spectra

5

Hot-carrier transfer

The resonant absorption of light in a metal nanoparticle leads to the formation of hot-electrons and holes. These hot-carriers can catalyze chemical reactions by occupying the orbitals of nearby molecules. In the direct hot-carrier transfer process which is the object of study in this chapter, the hot-carriers form directly in the molecular orbitals due to the decay of the initial plasmon excitation.

In the simulations in this chapter, a Ag_{201} NP is excited by an ultra-short laser pulse at the LSPR frequency ω_{pulse} . The dynamics of plasmon formation and decay into hot-carriers are resolved within the 30 fs of time propagation. Simulations are repeated with a CO molecule at different positions relative to the NP. At the end of the time propagation the fraction of hot-carriers formed in the direct hot-electron and hot-hole transfer processes are measured. Thus the probabilities of the direct hot-carrier transfer processes are calculated for many configurations of the NP and molecule.

A similar study has been conducted by Kumar *et al.*¹⁴, where a CO molecule was placed at the equilibrium distance from a Ag_{147} icosahedron. The probabilities of direct hot-electron and hot-hole transfer were 0.9–2.0 % and 0.2–0.5 % respectively. This thesis extends the study of Kumar *et al.*, calculating the transfer probabilities as a function of distance.

The chapter is structured as follows. In section 5.1 transition probabilities and hot-carrier distributions are defined in terms of quantities extracted from the TDDFT calculations. They are used to illustrate the process of plasmon formation and decay in the bare Ag_{201} NP. Section 5.2 introduces the NP + CO system. A few sites on the NP are selected as positions that the molecule approaches, and binding energy calculations are performed. A Voronoi mapping is done to assign each KS state to either the NP or the molecule (or partially to both). The Voronoi map makes it possible to divide the total transitions into transitions from or to NP or molecule. The aim is to separate the direct hot-electron transfer (transitions from the NP to the molecule) and the direct hot-hole transfer (transitions from the molecule to the NP) from transitions within the NP and within the molecule. After presenting the probabilities of hot-carrier transfer as a function of distance the projected densities of state (PDOS) for the NP and molecule are analyzed to explain the results. Section 5.3 discusses possibilities to tune parameters of the NP and molecule to obtain desirable traits in hot-carrier devices. For future studies, a proof-of-concept probe orbital that can take the role of any molecular orbital is introduced.

The DFT and TDDFT parameters in this chapter are set to the same values as in chapter 4; the grid spacing is 0.3 Å, vacuum size at least 6 Å and time step

10 as. The pulse has a full width at half maximum (FWHM) of 0.73 eV.

In chapter 4 the GLLB-SC xc -functional was used because predicts the location of the Ag d-band better than functionals without a derivative discontinuity. A similar density of states can also be obtained with PBE with a Hubbard +U correction on the Ag d-electrons. Here, GLLB-SC and PBE+U are employed to calculate hot-carrier distributions. Figure 5.1 shows the densities of state with GLLB-SC, PBE and PBE+U. The value $U = 3.5$ eV has been chosen as it most closely reproduces the GLLB-SC Ag DOS. Figure 5.2 shows that the peak frequency is similar with GLLB-SC and PBE+U. Energy calculations are done with the PBE xc -functional without +U as GLLB-SC is a potential functional without a well-defined energy.

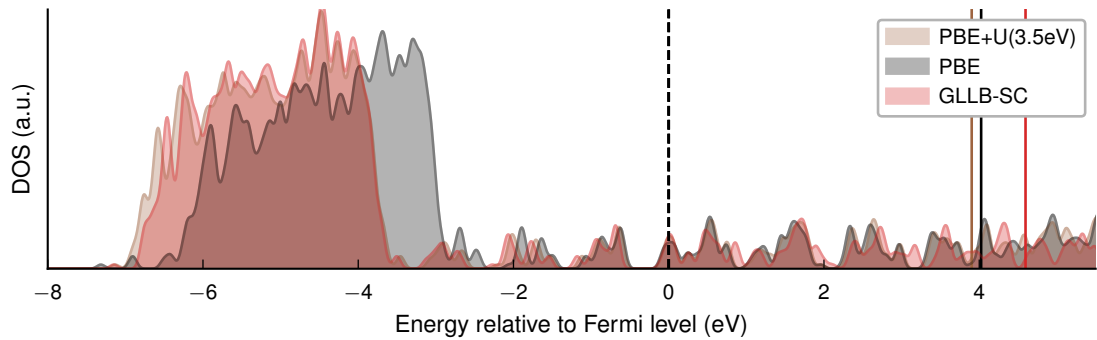


Figure 5.1: Density of states for the bare Ag_{201} RTO with the GLLB-SC, PBE and PBE+U xc -functionals. The parameter $U = 3.5$ eV reproduces the GLLB-SC DOS fairly well, while pure PBE overestimates the energy of the d-band edge. The dashed and solid lines mark the Fermi and vacuum levels respectively.

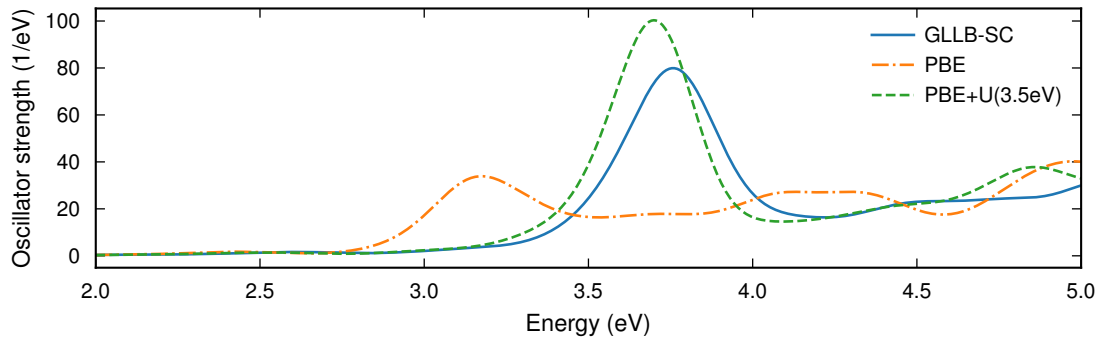


Figure 5.2: Photoabsorption spectrum of the bare Ag_{201} RTO calculated with PBE, PBE+U and GLLB-SC. Similar results are obtained with GLLB-SC and PBE+U, but PBE underestimates the LSPR frequency.

5.1 Hot-carrier dynamics for the bare NP

A central quantity for analyzing the hot-carrier dynamics in this chapter is the transition probability $P_{ia}(t)$. It is expressed in terms of occupation numbers f_i and the induced KS density matrix elements $\delta\rho_{ia}(t)$ defined in section 3.2.1

$$P_{ia}(t) = \left| \frac{\delta\rho_{ia}(t)}{\sqrt{f_i - f_a}} \right|^2. \quad (5.1)$$

The transition probability $P_{ia}(t)$ is well-defined for pairs of KS states i and a where $f_i > f_a$. By interpreting the occupied KS states as electrons and unoccupied KS states as holes, each matrix element $P_{ia}(t)$ is interpreted as the probability of the electron i being in state a at time t . The matrix can be visualized by constructing a transition contribution map (TCM)

$$M(t, \varepsilon_o, \varepsilon_u) = \sum_{ia}^{f_i > f_a} P_{ia}(t) g_i(\varepsilon_o) g_a(\varepsilon_u) \quad (5.2)$$

$$g_i(\varepsilon) = \frac{1}{2\pi\sigma^2} \exp\left(-\frac{(\varepsilon - \varepsilon_i)^2}{2\sigma^2}\right) \quad (5.3)$$

with a broadening parameter σ .

Figure 5.3 shows the TCM $M(t, \varepsilon_o, \varepsilon_u)$ with $\sigma = 0.07$ eV and corresponding induced densities, evaluated at a few time instances for the bare Ag₂₀₁ RTO. The snapshots at 11.3 fs, 11.6 fs and 11.9 fs correspond to the dipole moment taking its largest positive value, the value zero, and its largest (in magnitude) negative value. When the dipole moment is large in magnitude the density is collectively shifted along the polarization direction of the pulse, similar to the conceptual picture of the localized surface plasmon. The collective shift stems from transitions of s-electrons from states at approximately -1 eV³⁸, which can be seen in the TCM. In silver the plasmon is screened by d-electrons³⁸. This can be seen in the induced density centered around each atom counteracting the collective oscillation, and in the TCM as transitions from approximately -4 eV.

After the pulse has ended, the screened plasmon starts to decay into transitions resonant with the pulse, that is where $\varepsilon_a - \varepsilon_i = \hbar\omega_{\text{pulse}}$. This can be seen in the magnitude of the dipole moment oscillations decreasing. At 21.6 fs some of the s-electron transitions making up the plasmon remain, while at the end of the time propagation $t_{\text{end}} = 30$ fs all transitions are resonant with the pulse.

The transition probability can be summed into a probability of holes $P_i^h(t)$ or electrons $P_a^e(t)$ which corresponds to projecting the TCM on the electron or hole energy axes

$$P_i^h(t) = \sum_a^{f_i > f_a} P_{ia}(t), \quad P_a^e(t) = \sum_i^{f_i > f_a} P_{ia}(t) \quad (5.4)$$

$$M^h(t, \varepsilon_o) = \sum_i P_i^h(t) g_i(\varepsilon_o), \quad M^e(t, \varepsilon_u) = \sum_a P_a^e(t) g_a(\varepsilon_u). \quad (5.5)$$

At $t = 30$ fs the transition probabilities are close to (but not exactly at) the diagonal $\varepsilon_a - \varepsilon_i = \hbar\omega_{\text{pulse}}$. Because both the pulse and absorption spectrum have a finite width

there are also transitions with close to $\hbar\omega_{\text{pulse}}$ in energy difference. For reference, the pulse FWHM is 0.73 eV. Thus the distributions of holes and electrons should be similar save for a constant shift of $\hbar\omega_{\text{pulse}}$. They are shown in figure 5.4.

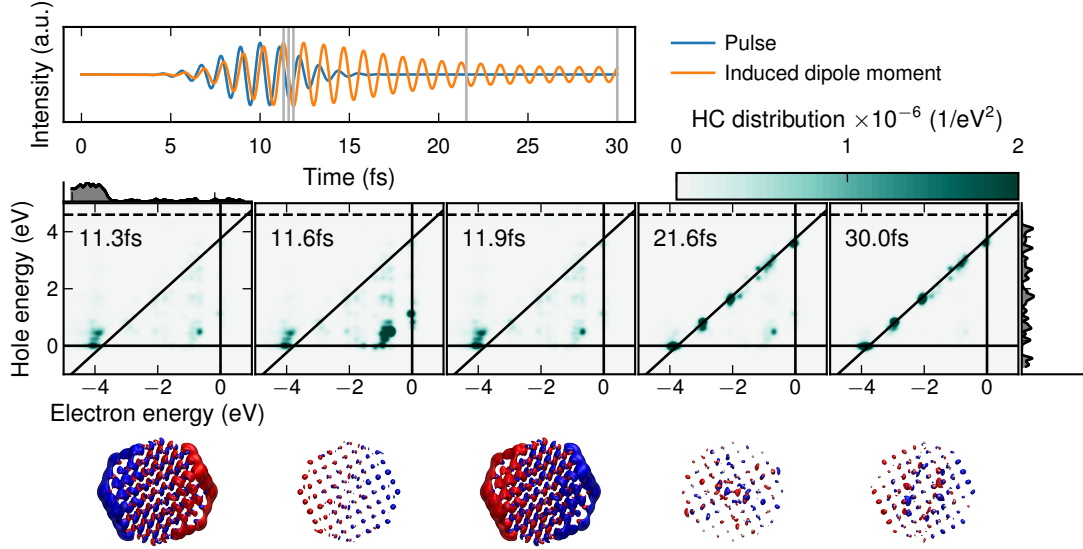


Figure 5.3: TCMs $M(t, \varepsilon_o, \varepsilon_u)$ to the transition probability $P_{ia}(t)$ with broadening parameter $\sigma = 0.07$ eV and GLLB-SC xc -functional. The solid vertical and horizontal lines indicate the position of the Fermi level on the hole and electron energy axes respectively. The dashed line indicates the vacuum level. The diagonal line indicates transitions where the energy difference equals the pulse frequency.

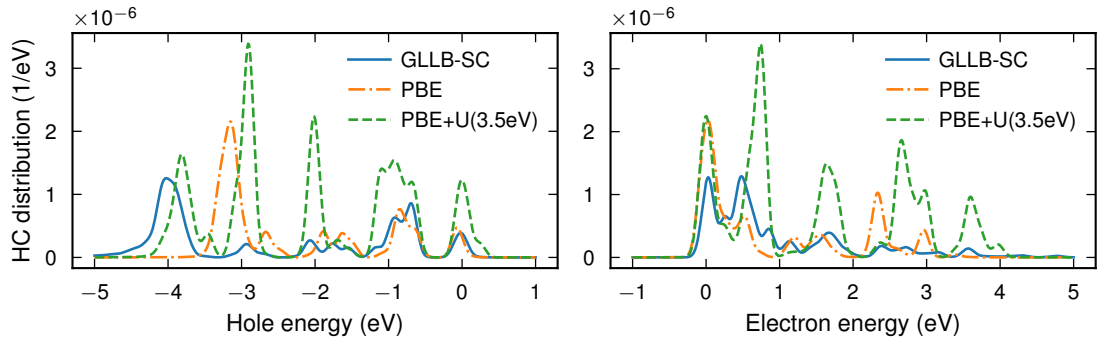


Figure 5.4: Projection of the hot-carrier distribution $M(t, \varepsilon_o, \varepsilon_u)$ at $t = 30$ fs on the electron and hole energy axes $M^h(t, \varepsilon_o)$ and $M^e(t, \varepsilon_u)$. As all transitions are resonant with the pulse, the electron and hole distributions have similar shapes. For earlier time instances when the non-resonant transitions have not yet decayed this would not be true.

5.2 Hot-carrier transfer across CO-NP interface

The CO molecule is chosen as a system of study for hot-carrier transfer across interfaces. It is placed at varying distances from four different sites on the Ag₂₀₁ RTO, illustrated in figure 5.5. The binding energy as a function of distance is computed for all four sites, and hot carrier distributions as a function of distance are computed for the two most strongly binding sites.

The RTO surface is made up of eight equivalent $\{111\}$ faces and six equivalent $\{100\}$ faces. On the $[111]$ face the *on-top* site is right on top of the atom in the middle of the face, and for the *fcc* site the position is shifted to the nearest hollow between three Ag atoms. On the $[100]$ face the *hollow* site denotes the position between two atoms, as close to the middle of the face as possible. For each of the aforementioned sites the molecule is oriented with the carbon atom facing the NP and the bond axis perpendicular to the face. The distance is measured between the carbon atom and the plane of Ag atoms in the face.

In the *corner* site configuration the CO is by a corner atom between the $[100]$ face and the two neighboring $\{111\}$ faces. The bond axis of the molecule is aligned with a line from the nearest corner atom and the corner atom on the opposite side of the NP. Distance is measured between the C atom and corner Ag atom.

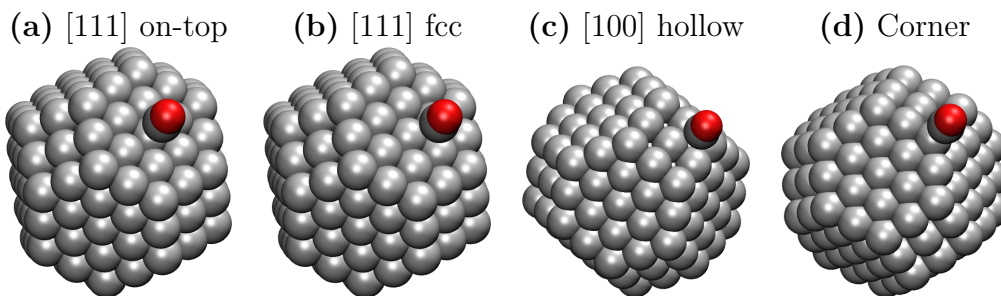


Figure 5.5: The four considered sites of CO adsorption are (a) between three atoms on a $[111]$ face (*fcc site*), (b) in the middle of the $[111]$ face (*on-top site*), (c) between two atoms on the $[100]$ face and (d) in the corner between the $[100]$ and two $\{111\}$ faces.

5.2.1 Binding energies as a function of distance

For each site and distance between NP and molecule the binding energy is calculated from three ground state calculations, one with the total system NP+CO, one with the bare NP and one with the bare CO molecule

$$E_{\text{bind}}(\text{site}, d) = E_{\text{NP+CO}}(\text{site}, d) - E_{\text{NP}} - E_{\text{CO}}. \quad (5.6)$$

The bare molecule calculation corresponding to each distance d is performed with the molecule in the same position as in the total system calculation. LCAO basis functions are placed at the positions corresponding to each Ag atom in the total system. This is done to eliminate egg-box and basis set superposition errors. The

same procedure, with basis functions at the positions corresponding to the C and O atoms, is done for the bare NP calculations.

With the present definition of the binding energy negative values $E_{\text{bind}}(\text{site}, d)$ imply that it is energetically favorable for the molecule and NP to be separated by a distance d than to be entirely isolated. Local minima in E_{bind} are positions where the molecule might get stuck for some time.

Figure 5.6 shows the binding energy as a function of distance for the four sites. The corner site shows the strongest binding, with a minimum of -0.35 eV at a distance of 2.2 Å. The [111] on-top site is barely bound with a minimum of -0.02 eV at $d = 2.2$ Å. The [111] fcc and [100] hollow sites show initial repulsion below 3 Å which flattens out around 2 Å.

Based on this information the molecule is expected to be near the corner site and [111] on-top site the most of the time. These sites are chosen for the hot-carrier analysis. It is however important to keep in mind that a real CO molecule is always in thermal motion and may overcome barriers in the binding energy, and move laterally or wiggle which the present analysis does not cover. A repulsion starts to be strong below 1.8 Å this is the smallest distance studied.

At large separations the binding energies approach zero, indicating that the NP and adsorbate do not interact. At small separations there is very strong repulsion due to the orbitals of the two systems starting to overlap. The repulsion starts at the largest separations for the corner and on-top sites, ~ 0.5 Å closer for the fcc site and yet ~ 0.5 Å closer for the hollow site. This behaviour is consistent with the geometry of the sites. In the two former cases the approach happens straight on a Ag atom, with the latter approaching the hollow space between two and three Ag atoms.

Metallic NPs are known to contract with decreasing size because of the under coordinated surface atoms preferring tighter bonds⁴⁴. Considering the same adsorption curve calculation for NPs that have been artificially strained may therefore indicate the behavior for other sizes. Figure 5.7 shows how adsorption to the [111] on-top site depends on tensile and compressive strains of 1 and 2%. The adsorption minimum becomes deeper for tensile strain, suggesting that adsorption may occur more easily on larger NPs.

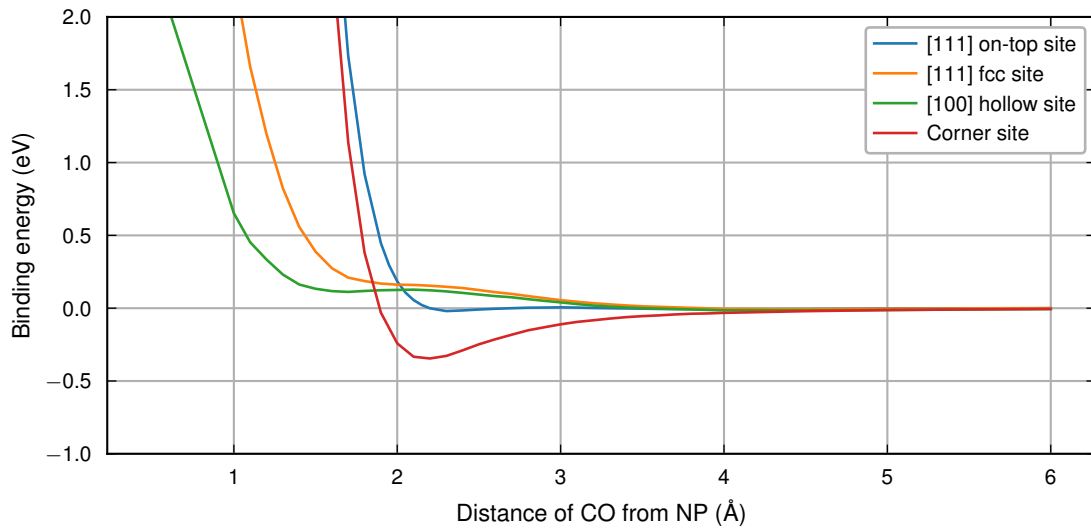


Figure 5.6: Binding energy curves for the four adsorption configurations. The corner and [111] on-top sites show negative binding energies (the on-top minimum being much weaker) around a minimum, meaning that adsorption is favorable. Binding to the [100] hollow and [111] fcc sites is not energetically favorable but local minima appear.

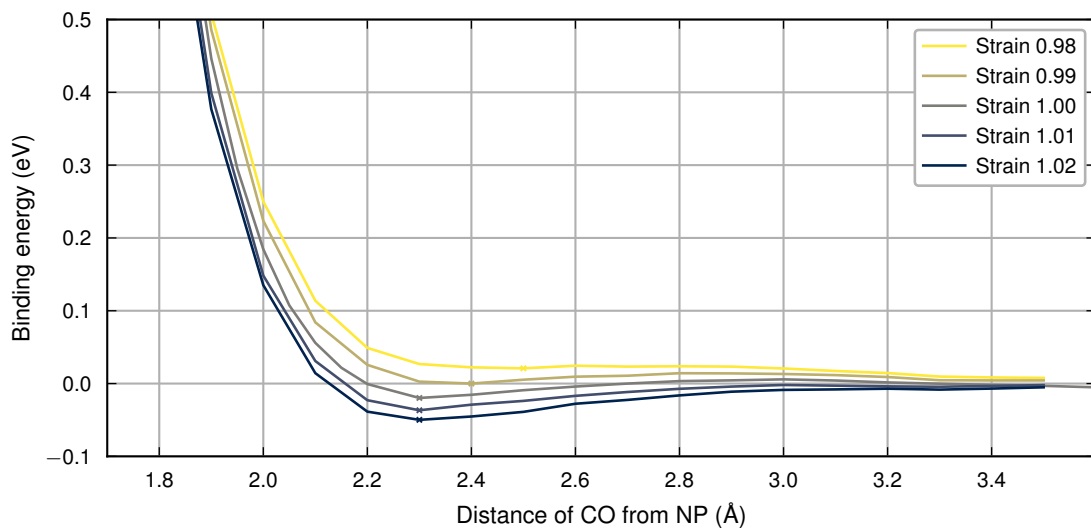


Figure 5.7: Binding energy curves for strained NPs in the [111] on-top configuration. The energy minima are marked with small crosses. From the figure it appears that tensile strain increases the depth of the adsorption minimum, while compressive strain weakens it.

5.2.2 Projected densities of state

The next step of the analysis is to assign each KS ground state $\phi_i^{(0)}(\mathbf{r})$ to either the CO molecule, the Ag NP or partially to both. This is done by constructing a *Voronoi decomposition* of space

$$a(\mathbf{r}) = \begin{cases} \text{CO} & \text{if } \mathbf{r} \text{ closer to any CO atom than any NP atom} \\ \text{NP} & \text{else.} \end{cases} \quad (5.7)$$

The function $a(\mathbf{r})$ takes the value CO or NP, which numerically can be represented with any unique integer. It is straightforward to generalize the decomposition into a decomposition around each atom, or any group of atoms, but this is not necessary for the present analysis.

Next, a weight w_i^b is assigned to each $\phi_i^{(0)}(\mathbf{r})$

$$w_i^b = \int d\mathbf{r} \left| \phi_i^{(0)}(\mathbf{r}) \right|^2 \delta_{a(\mathbf{r}),b}, \quad (5.8)$$

where the Kronecker delta $\delta_{a(\mathbf{r}),b}$ takes the value 1 if $a(\mathbf{r})$ is the same identifier as b and 0 otherwise. At large separations between the CO and NP we can expect the weights to be either 0 or 1, meaning that the ground state KS orbitals are localized to either of them. By construction, the Voronoi weights sum to one $w_i^{\text{CO}} + w_i^{\text{NP}} = 1$ for each state i .

We define the projected densities of state (PDOS)

$$D^b(\varepsilon) = \sum_i w_i^b g_i(\varepsilon). \quad (5.9)$$

Their sum is the total DOS $D^{\text{CO}}(\varepsilon) + D^{\text{NP}}(\varepsilon) = D(\varepsilon)$.

The molecular PDOS $D^{\text{CO}}(\varepsilon)$ shows strong distance dependence, which is seen for the [111] on-top site with GLLB-SC *xc*-functional in figure 5.8. At large separations $d = 6 \text{ \AA}$ the PDOS resembles the DOS of a bare CO molecule. The highest occupied molecular orbital (HOMO) is a σ -type state at 4.7 eV below Fermi level and the lowest unoccupied molecular orbital (LUMO) is a doubly degenerate π -type state at 3.0 eV above Fermi level.

As the separation between NP and molecule decreases the molecular states shift to lower energies. There are indications that the shifts between $d = 6 \text{ \AA}$ and 4 \AA , which are approximately 0.1 eV, could be attributed to a basis set superposition error. The shifts below 4 \AA are greater in magnitude and more likely a real effect. Particularly the energy of the HOMO state changes rapidly and crosses the next highest occupied molecular orbital at 2.1 \AA . As the HOMO and LUMO states hybridize with the NP at small separations the states split into several branches. The total number of electrons in the hybridized HOMO and LUMO branches, *i.e.* the integral of the PDOS in a region, is constant as a function of distance. This splitting into several states as the molecule approaches the NP occurs earliest and most strongly for the LUMO state.

Of direct relevance for the hot-carrier transfer are only the states within the pulse energy $\pm \hbar\omega_{\text{pulse}}$ of the Fermi level, as transfer can only occur between occupied and unoccupied states. Note that the HOMO state is outside this range, however some of the hybridized HOMO-like branches at small separations are in range.

The NP PDOS $D^{\text{NP}}(\varepsilon)$ on the other hand, shows little distance dependence, and as seen in figure 5.1 there is little difference between the GLLB-SC and PBE+U, $U = 3.5\text{ eV}$ *xc*-functionals. In this chapter it is thus treated as constant, which somewhat simplifies the analysis.

Figure 5.9 shows the distance dependence of the molecular PDOS for both *xc*-functionals and sites. The HOMO state seems to behave similarly in all cases. The energy of the LUMO state is at all separations lower by almost 1 eV with PBE+E compared to GLLB-SC. For both functionals the same trend is seen between the two sites; at small separations the LUMO state has a lower energy on the corner site than at the [111] on-top site, but at large separations there is no difference between sites.

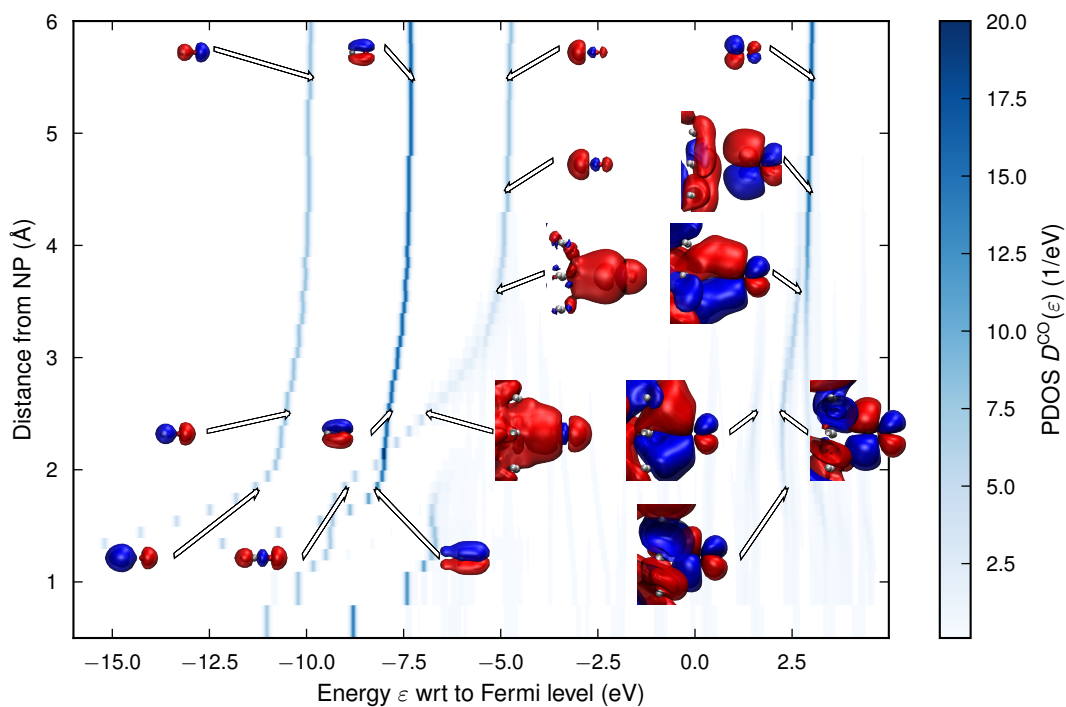


Figure 5.8: Molecular PDOS for the [111] on-top site with GLLB-SC functional. The overlays of isosurfaces show the character of the corresponding KS wave functions. At large separations the PDOS shows four distinct peaks. The states at 3.0 eV (LUMO) and at -7.3 eV are doubly degenerate, which is seen as the PDOS being twice as large as for the other states. As the separation decreases the state energies are lowered. Particularly the LUMO but to some extent also the HOMO become delocalized and spread over a span of energies as they hybridize with the NP states.

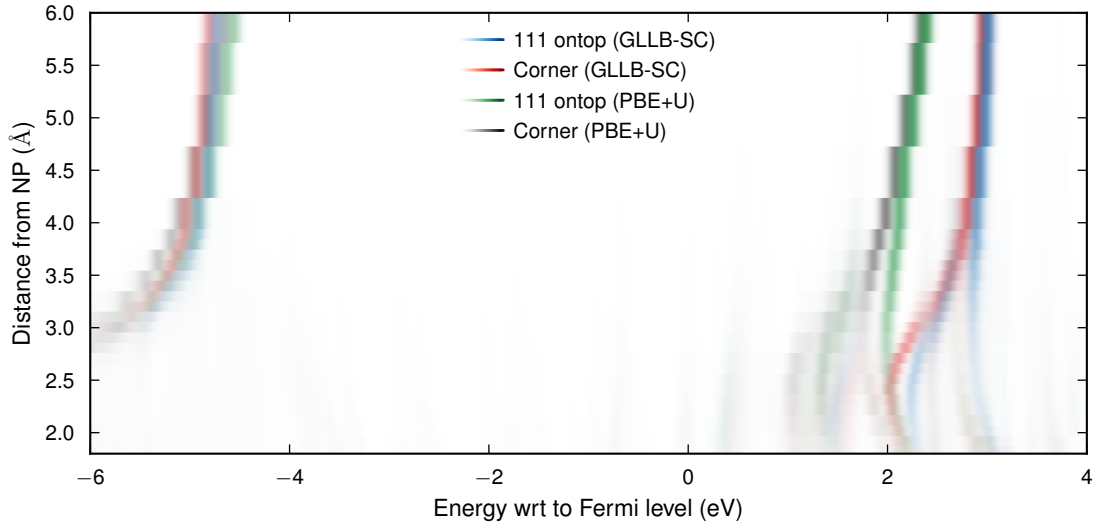


Figure 5.9: Molecular PDOS for the [111] on-top site and corner site, with both xc -functionals. Both sites show a similar PDOS at large NP-molecule separations. PBE+U gives a LUMO level that is lower by almost 1 eV than the GLLB-SC LUMO level.

5.2.3 Hot-carrier distributions after plasmon decay

With the Voronoi weights w_i^b we define the partial hot-carrier transition probabilities between KS states i and a

$$P_{ia}^{b \rightarrow b'}(t) = P_{ia}(t)w_i^b w_a^{b'}. \quad (5.10)$$

Electron and hole distributions for the partial processes are formed analogously to the full distributions.

The transition probabilities reach stationary values after the plasmon has fully decayed. We define the process probabilities of the processes $\text{NP} \rightarrow \text{NP}$, $\text{NP} \rightarrow \text{CO}$, $\text{CO} \rightarrow \text{NP}$, and $\text{CO} \rightarrow \text{CO}$ as the fraction of transitions of each type over the total transitions at the end of the time propagation t_{end}

$$T^{b \rightarrow b'} = \frac{\sum_{ia} P_{ia}^{b \rightarrow b'}(t_{\text{end}})}{\sum_{ia} P_{ia}(t_{\text{end}})}. \quad (5.11)$$

The process probabilities $T^{\text{NP} \rightarrow \text{CO}}$ and $T^{\text{CO} \rightarrow \text{NP}}$, corresponding to the direct hot-electron and hot-hole transfer processes respectively, are shown as a function of distance, site and xc -functional in figure 5.10. The corresponding partial hot-carrier distributions $P^{h,b \rightarrow b'}(t_{\text{end}}, \varepsilon_o)$, $P^{e,b \rightarrow b'}(t_{\text{end}}, \varepsilon_u)$ for the [111] ontop site and GLLB-SC functional are shown as a function of distance in figure 5.11.

Direct hot-electron transfer (transitions $\text{NP} \rightarrow \text{CO}$) amounts for around 1-2% of all transitions in a wide range of distances. Below 4 Å there seems to be no clear trend in the process probability with respect to site or functional. For example the GLLB-SC functional predicts twice as much transfer for the [111] on-top site

at $d = 3.8 \text{ \AA}$ than at $d = 1.8 \text{ \AA}$. The hot-carrier distributions in figure 5.11a show that the GLLB-SC [111] on-top transfer maximum at 3.8 \AA consists of transitions from -0.7 eV to 2.9 eV . At smaller separations there are also hot-holes at -2.1 eV and -1.5 eV and corresponding hot-electrons at 1.6 eV and 2.3 eV , but their total amount is smaller than the amount of transitions at $d = 3.8 \text{ \AA}$. For separations over $4-4.5 \text{ \AA}$ the transfer probability decreases with increasing distance and there seems to be less difference between two sites with the same functional.

Direct hot-hole transfer (transitions $\text{CO} \rightarrow \text{NP}$) amounts for between 0.2-0.3% of all transitions at $d = 1.8 \text{ \AA}$. The contribution decreases almost monotonically for both sites and functionals with increasing separation. For the GLLB-SC [111] on-top site figure 5.11b shows contributions from several transitions. At small separations the largest contribution is from a transition -0.7 eV to 2.9 eV . Near 4 \AA the sole contribution is from a transition -2.9 eV to 0.9 eV .

Intra molecular transitions ($\text{CO} \rightarrow \text{CO}$) peak at small separations with a probability of 100 ppm for the [111] on-top site and 50 ppm for the corner site, decaying to zero at separations larger than 4 \AA . As the probabilities are small they are not shown.

Intra nanoparticle transitions ($\text{NP} \rightarrow \text{NP}$) make up the remaining 98 - 99%. Their distribution is close to the distribution for bare NPs shown in figure 5.4.

In previous work by Kumar *et al.*¹⁴ an Ag_{147} icosahedron (NP with only [111] surfaces) with CO at an equilibrium distance has been studied. The GLLB-SC *xc*-functional and a similar time propagation scheme was employed. Kumar *et al.* report direct hot-electron and hot-hole transfer probabilities of 0.9-2.0% and 0.2-0.5% respectively, depending on adsorption site, which is in line with the results here.

The accuracy of the *xc*-functional is an important question that is beyond the scope of this thesis. As shown in the reminder of this section, the appearance of the hot-carrier distributions is largely determined by the molecular and NP PDOS. Thus to obtain accurate transfer probabilities, accurate PDOSes are required. Those could be retrieved from higher level theory or experiments.

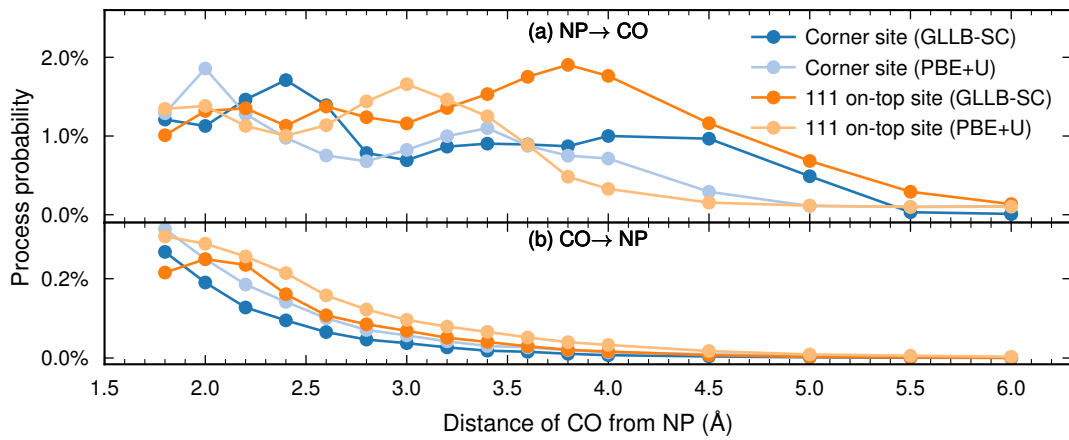


Figure 5.10: Probabilities of hot-carrier transfer processes as a function of the separation between the NP and CO molecule. (a) Direct hot-electron and (b) hot-hole transfer process.

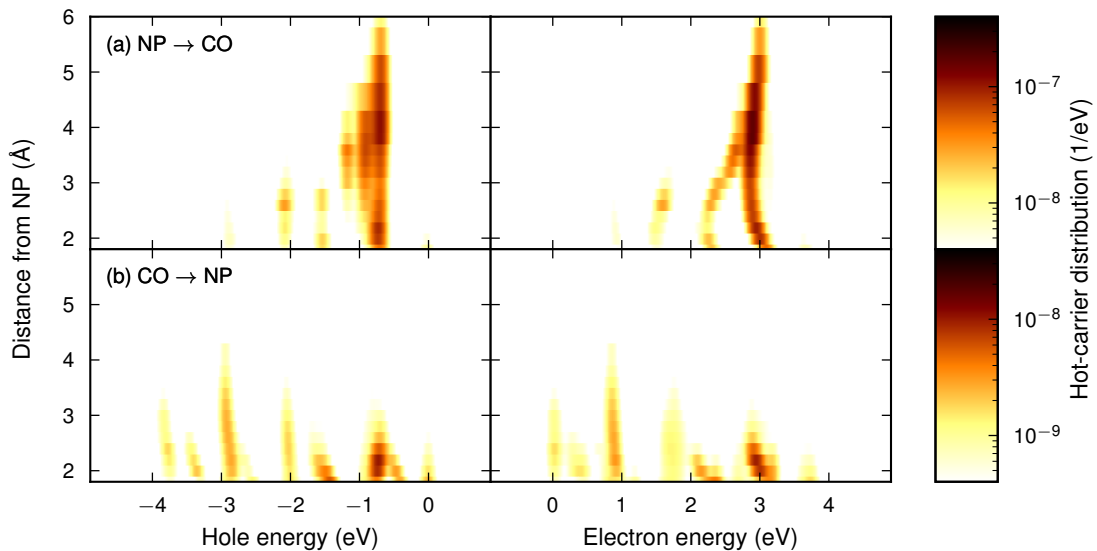


Figure 5.11: GLLB-SC [111] on-top site hot-hole and hot-electron distributions. (a) Direct hot-electron and (b) hot-hole transfer process.

5.2.3.1 Direct hot-electron transfer

In this section it is shown that the particular appearance of the hot-carrier distributions for the direct hot-electron transfer process (NP \rightarrow CO) can be attributed to the alignment between the NP PDOS $D^{\text{NP}}(\varepsilon)$ and the distance dependent molecular PDOS $D^{\text{CO}}(\varepsilon)$. While this dependence is general for both sites and xc -functionals the analysis is visualized for the [111] on-top configuration with the GLLB-SC functional as an example. The sensitivity of the hot-carrier distributions to the molecule PDOS is the cause for the varying transfer probabilities with adsorption site and xc -functional.

Figure 5.12 shows the hot-hole distribution in the NP on the same energy axis as the NP PDOS and the hot-electron distribution in the molecule on the same energy axis as the molecular PDOS. As described earlier the hot-hole and hot-electron distributions are similar (but not identical, due to the finite pulse width) albeit shifted by the pulse energy $\hbar\omega_{\text{pulse}}$.

An observation from figure 5.12 is that the molecular state around 3 eV (to the left of the rightmost blue guide line) is aligned with a peak in the NP PDOS. The neighboring molecular state which is present at $d < 3 \text{ \AA}$ slightly above 2 eV is aligned with a gap in the NP PDOS. Thus, even though the molecular PDOS is higher at the latter state, the corresponding HC distributions are lower. When the densities of these two states coincide around $d = 4 \text{ \AA}$ the HC transfer is maximal.

The importance of the alignment between NP and molecular PDOS is highlighted by plotting the joint density of states (JDOS)

$$J^{\text{NP,CO}}(\varepsilon) = D^{\text{NP}}(\varepsilon - \hbar\omega_{\text{pulse}})D^{\text{CO}}(\varepsilon) \quad (5.12)$$

in figure 5.13. In the interval $0 < \varepsilon < \hbar\omega_{\text{pulse}}$ the JDOS looks as an approximation to both the hot-hole and hot-electron distributions. Outside this interval transitions cannot occur. For example the JDOS reproduces the gap in the hot-hole distribution at $\sim -1.5 \text{ eV}$ (corresponding to the gap in the NP PDOS) which is not seen in the molecular PDOS alone.

Such a simplified JDOS does not capture effects from the finite width of the pulse, which leads to hot-hole and hot-electron distributions differing. Neither does it capture the decay of the hot-carrier distributions above $d = 4 \text{ \AA}$ due to the spatial overlap between states decaying. Also, as the JDOS is constructed using ground state DFT quantities only, it should not be expected to predict the coupling strength of the plasmon to different electron-hole transitions correctly. Despite these limitations the JDOS appears to approximate the hot-carrier distributions well.

5.2.3.2 Direct hot-hole transfer and other processes

The dependence of the hot-carrier distributions on the PDOS alignment apply equally to the hot-hole transfer process and for NP \rightarrow NP and CO \rightarrow CO transitions. Here the JDOS of interest are respectively:

$$J^{\text{CO,NP}}(\varepsilon) = D^{\text{CO}}(\varepsilon - \hbar\omega_{\text{pulse}})D^{\text{NP}}(\varepsilon) \quad (5.13)$$

$$J^{\text{NP,NP}}(\varepsilon) = D^{\text{NP}}(\varepsilon - \hbar\omega_{\text{pulse}})D^{\text{NP}}(\varepsilon) \quad (5.14)$$

$$J^{\text{CO,CO}}(\varepsilon) = D^{\text{CO}}(\varepsilon - \hbar\omega_{\text{pulse}})D^{\text{CO}}(\varepsilon). \quad (5.15)$$

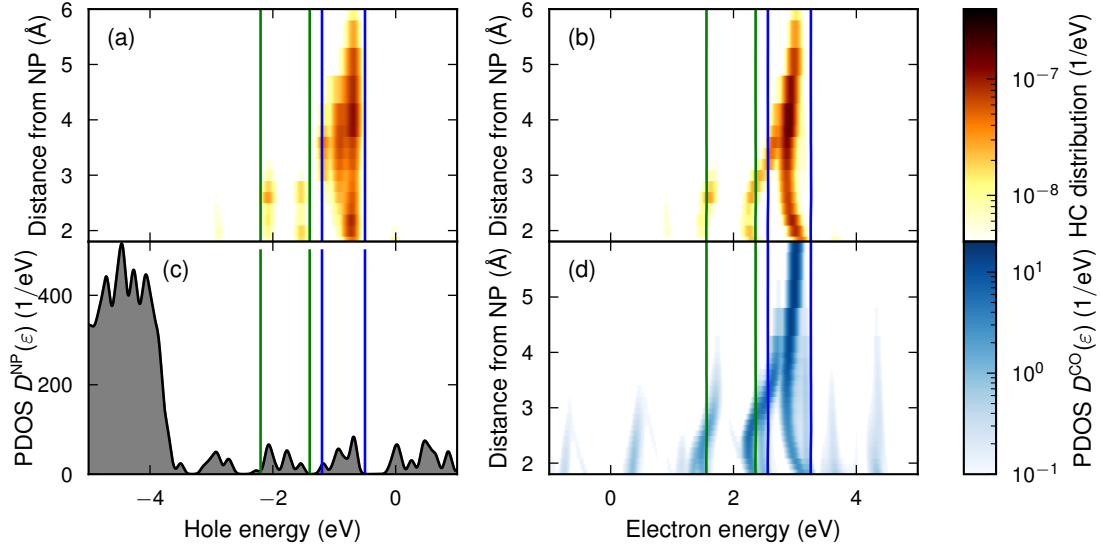


Figure 5.12: GLLB-SC [111] on-top site hot-carrier distributions for the direct hot-electron transfer process in relation to NP and molecular PDOS. (a) Hot-hole and (b) hot-electron distributions as a function of distance. (c) The NP PDOS, which is practically independent of distance. (d) The molecular PDOS as a function of distance. To aid the eye, green and blue lines are drawn at a few energies in panels (a) and (c) and at energies higher by $\hbar\omega_{\text{pulse}}$ in panels (b) and (d).

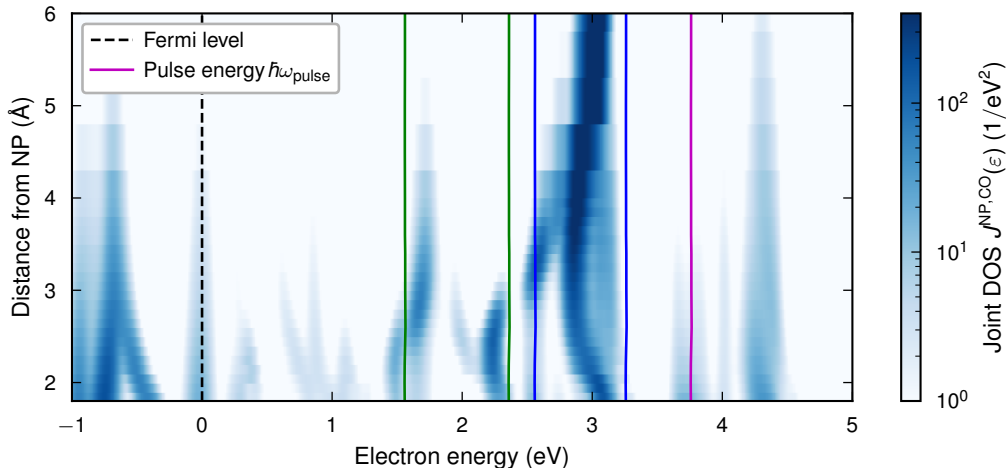


Figure 5.13: GLLB-SC [111] on-top site joint density of states related to the direct hot-electron transfer process. This quantity shows how the hot-electron distribution (and hot-hole distribution shifted by $\hbar\omega_{\text{pulse}}$) would look if it only depended on the product of overlapping projected densities of state. The hot electrons are required to be between the Fermi level and the pulse energy, which are marked in the figure.

The two most striking differences between the direct hot-hole transfer and hot-electron transfer processes is that the former happens at most with one fifth of the probability of the latter, and that its probability decays more rapidly with distance. With the [111] on-top GLLB-SC site as an example, figure 5.14 relates the NP and molecular PDOS to the direct hot-hole transfer process hot-carrier distributions. Figure 5.15 shows the JDOS $J^{\text{CO,NP}}(\varepsilon)$. It is seen that the molecular PDOS in the region ε from $-\hbar\omega_{\text{pulse}}$ to 0 is much lower than in the region 0 to $\hbar\omega_{\text{pulse}}$, and practically zero above 3 \AA . At small separations, the contributions to the molecular PDOS in the region $\hbar\omega_{\text{pulse}} \leq \varepsilon \leq 0$ are hybridized states originating from the HOMO. At large separations there is a large contribution in the JDOS at -1 eV from the non-hybridized HOMO state, which cannot contribute to the hot-carrier transfer because $\varepsilon < 0$.

It is worth noting here that the HOMO state at -1 eV in the JDOS presents an opportunity for engineering the system for increased hot-hole transfer. If one were to somehow raise the HOMO level with respect to the Fermi level by at least 1 eV , the hot-hole transfer process could be expected to be greatly enhanced.

The behavior of the NP \rightarrow NP and CO \rightarrow CO processes is also explained by a JDOS analysis, however corresponding figures are not shown. The low molecule PDOS in the region ε from $-\omega_{\text{pulse}}$ to 0 is the reason for the low rate of CO \rightarrow CO transitions, and the fact that the NP PDOS is non-zero almost everywhere is the reason for the high rate of NP \rightarrow NP transitions.

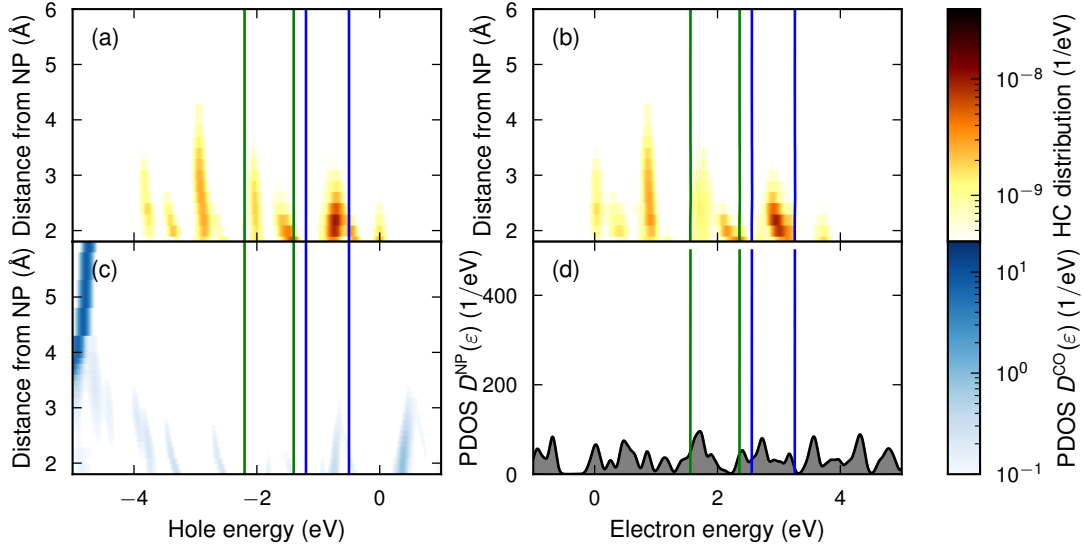


Figure 5.14: GLLB-SC [111] on-top site hot-carrier distributions for the direct hot-hole transfer process in relation to NP and molecular PDOS. (a) Hot-hole and (b) hot-electron distributions as a function of distance. (c) The molecular PDOS as a function of distance. (d) The NP PDOS, which is practically independent of distance. To aid the eye, green and blue lines are drawn at a few energies in panels (a) and (c) and at energies higher by $\hbar\omega_{\text{pulse}}$ in panels (b) and (d).

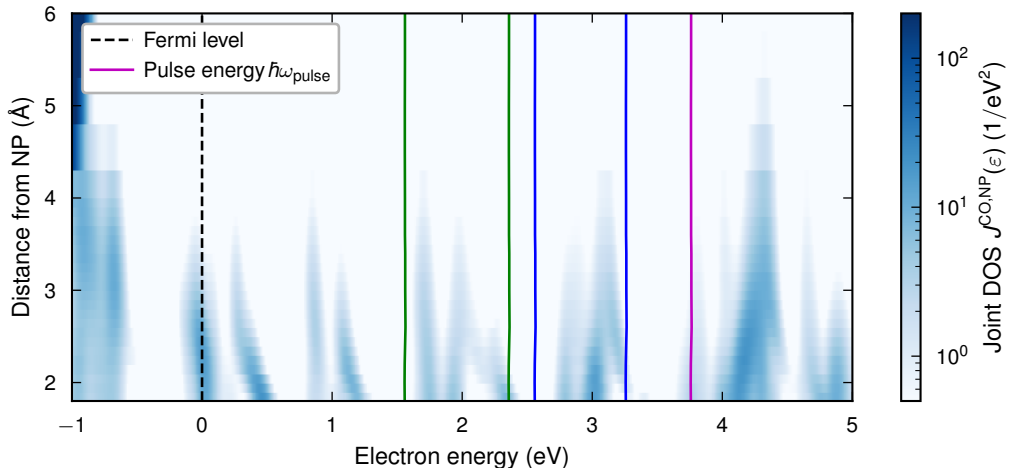


Figure 5.15: GLLB-SC [111] on-top site joint density of states related to the direct hot-hole transfer process. This quantity shows how the hot-electron distribution (and hot-hole distribution shifted by $\hbar\omega_{\text{pulse}}$) would look if it only depended on the product of overlapping projected densities of state. The hot electrons are required to be between the Fermi level and the pulse energy, which are marked in the figure.

5.3 Generalization and future considerations

The previous section has highlighted the importance of the alignment of donor and acceptor states for hot-carrier transfer. While other effects play a role the alignment roughly determines the shape of the hot-carrier distributions. The implications of this, and possibilities for applications are discussed in this section.

Figure 5.16 illustrates the process of hot-electron transfer. There are three variables in this picture – the position of the donor state in the NP $\varepsilon_{\text{donor}}$, the frequency of the light ω_{pulse} and the position of the acceptor LUMO level in the molecule $\varepsilon_{\text{LUMO}}$. The prerequisite for hot-carrier transfer is

$$\varepsilon_{\text{donor}} + \hbar\omega_{\text{pulse}} = \varepsilon_{\text{LUMO}}. \quad (5.16)$$

The size, shape, composition and environment of the NP affects the LSPR frequency, and thus the pulse frequency ω_{pulse} if high efficiency is desired. The electronic structure at the NP surface of interest (determining possible $\varepsilon_{\text{donor}}$ levels in the direct hot-electron transfer process) may be more sensitive to local structure and composition. For example by alloying or introducing local strain the NP energy levels could be shifted. The acceptor energy levels are determined by the type of molecule.

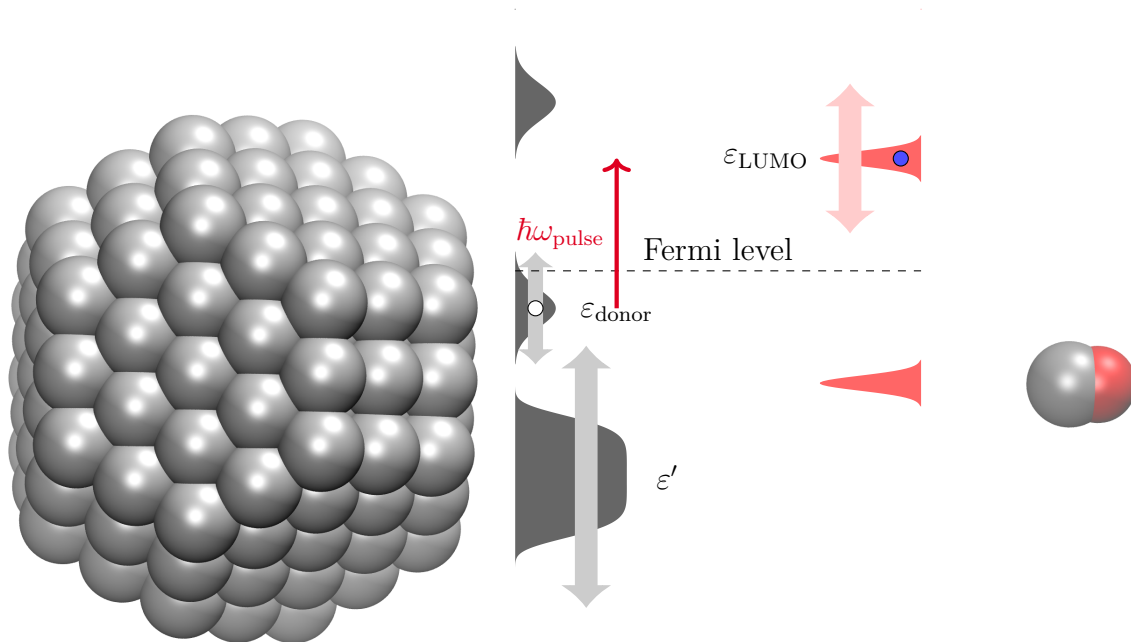


Figure 5.16: Schematic drawing of conditions required for hot-electron transfer. Hot-electron transfer can occur when $\varepsilon_{\text{donor}} + \hbar\omega_{\text{pulse}} = \varepsilon_{\text{LUMO}}$. By engineering these variables, hot-carrier transfer to certain orbitals may be favored or inhibited. The pulse frequency ω_{pulse} is set to the LSPR frequency, which is affected by NP size, shape, *etc.* The NP levels $\varepsilon_{\text{donor}}$, ε' may change by modifying the NP surface.

The ability to modify the LSPR frequency and electronic structure at the NP surface presents opportunities for engineering hot-carrier devices for specific

applications. A possible way to boost the probability of hot-electron transfer in the NP-CO system could be to shift the NP energy levels upwards so that transfer may occur from the large d-band.

For photocatalysis applications selectivity is a desired trait, *i.e.* the favoring of transfer to an orbital in one molecular species, but not to other. Achieving high selectivity in hot-electron transfer would require a sharp peak in the occupied part of the NP PDOS, that matches the LUMO state of the selected molecule.

For certain applications a high degree of charge separation may be desired, *i.e.* significantly more transfer of one type of charge carrier than the other. This can be achieved with a molecule (such as CO), where the states are well separated, or with a wide band gap semiconductor.

5.3.1 Probe orbital approach

A future direction in the study of hot-carrier transfer in NP-molecule systems could be the utilization of a probe orbital. As shown in the previous section, the PDOS is key to hot-carrier transfer. The idea is to replicate the PDOS of the relevant states of a real molecule (by for example consulting experiments or higher-level theory). Here, such a probe orbital is introduced as proof-of-principle.

An external potential on the form

$$v_{\text{ext}}(\mathbf{r}) = \begin{cases} d_{\text{probe}} \left[2 \left(\frac{|\mathbf{r}-\mathbf{r}_0|}{r_{\text{probe}}} \right)^2 - \left(\frac{|\mathbf{r}-\mathbf{r}_0|}{r_{\text{probe}}} \right)^4 - 1 \right] & , |\mathbf{r}_{\text{probe}} - \mathbf{r}_0| < r_{\text{probe}} \\ 0 & , \text{else} \end{cases} \quad (5.17)$$

is added to the system. The potential is centered at \mathbf{r}_0 and has a tunable depth d_{probe} and radius r_{probe} . The potential is approximately harmonic in the center of the well and is continuous and differentiable everywhere. Figure 5.17 shows the potential for different values d_{probe} .

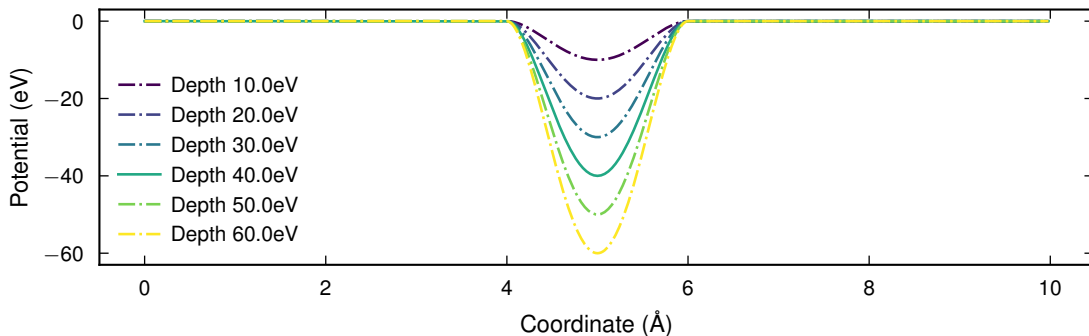


Figure 5.17: The potential used to implement the probe orbital. The radius is $r_{\text{probe}} = 1 \text{ \AA}$ and the different values of the depth d_{probe} are indicated in the legend.

A similar study of the hot-carrier transfer distance dependence as for the CO molecule is conducted with the probe orbital. The probe depth and radius are set to 40 eV and 1 \AA respectively. As the ground state calculations could not reliably be

converged with the GLLB-SC xc -functional PBE+U is used. Voronoi weights and a probe PDOS are constructed in the same way as for the molecule.

Figure 5.18 shows the distance dependent PDOS of the probe orbital approaching the [111] on-top site. Here, the distance d is measured between the center of the probe \mathbf{r}_0 and nearest Ag atom. For $d > 4.5 \text{ \AA}$ there is a single unoccupied state (that is spherically symmetric in contrast to the π -type LUMO state of CO). Its energy varies smoothly with distance between 1.5 eV and 3.3 eV. Below 4.5 \AA a hybridized probe orbital state forms around the Fermi level. Thus only values $d \geq 4.5 \text{ \AA}$ are considered further. The corner site PDOS (not shown) has a similar distance dependence, with a hybridized state forming at Fermi level for $d < 4.8 \text{ \AA}$.

Figure 5.19 shows the direct hot-electron transfer probability for the probe for the [111] on-top site and corner site. As the sole probe state with the present radius and width is above Fermi level, there is no hot-hole transfer for the considered distances. The direct hot-electron transfer has a wide peak around 6 \AA for both sites. For the [111] on-top site there is additionally a peak around 5 \AA .

Figure 5.20 shows the hot-carrier distribution in relation to the PDOS and figure 5.21 shows the JDOS for the [111] on-top site. Both of the previously mentioned maxima in the hot-carrier distributions for the [111] on-top site are correlated to the peaks in the NP PDOS aligning with the probe state. For the corner site (not shown) the probe PDOS does not reach the energy 2.2 eV at 5 \AA like the [111] on-top site does, and consequently lack the corresponding maximum in the HC transfer. This shows that the JDOS analysis framework works equally well for the NP+probe system as the NP+molecule system.

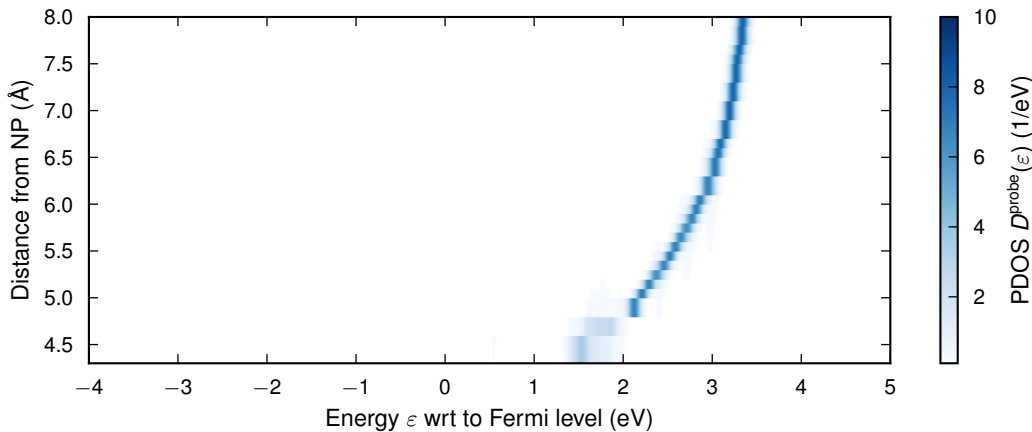


Figure 5.18: PDOS of the probe orbital $D^{\text{probe}}(\epsilon)$ for the [111] on-top site with the PBE+U xc -functional.

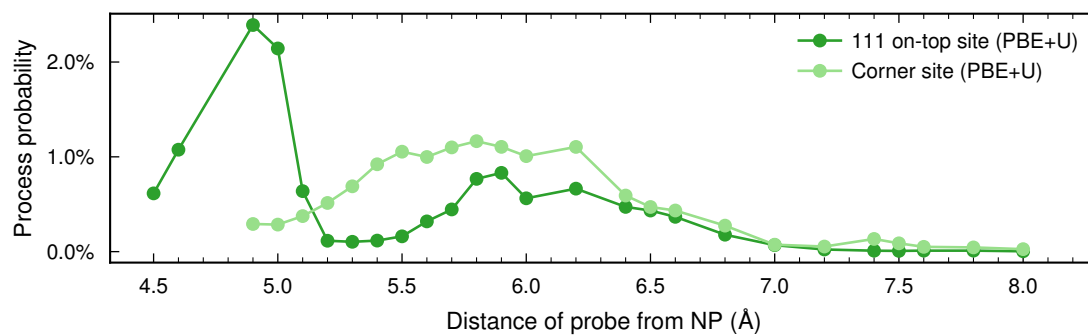


Figure 5.19: Probability of the direct hot-electron transfer process as a function of the separation between the NP and probe.

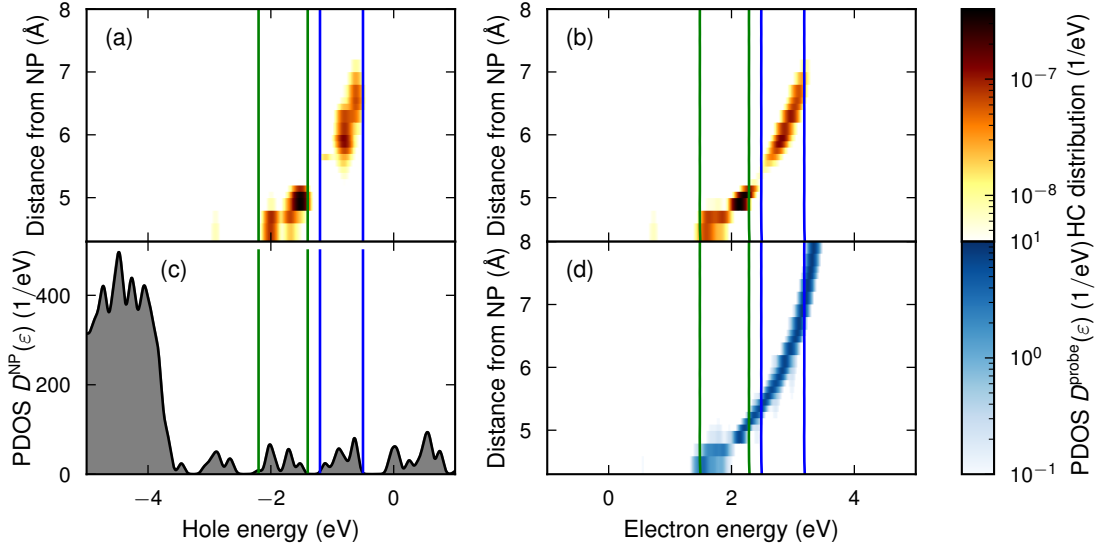


Figure 5.20: Probe orbital [111] on-top site hot-carrier distributions for the direct hot-electron transfer process in relation to NP and probe PDOS. (a) Hot-hole and (b) hot-electron distributions as a function of distance. (c) The NP PDOS, which is practically independent of distance. (d) The probe PDOS as a function of distance. To aid the eye, green and blue lines are drawn at a few energies in panels (a) and (c) and at energies higher by $\hbar\omega_{\text{pulse}}$ in panels (b) and (d).

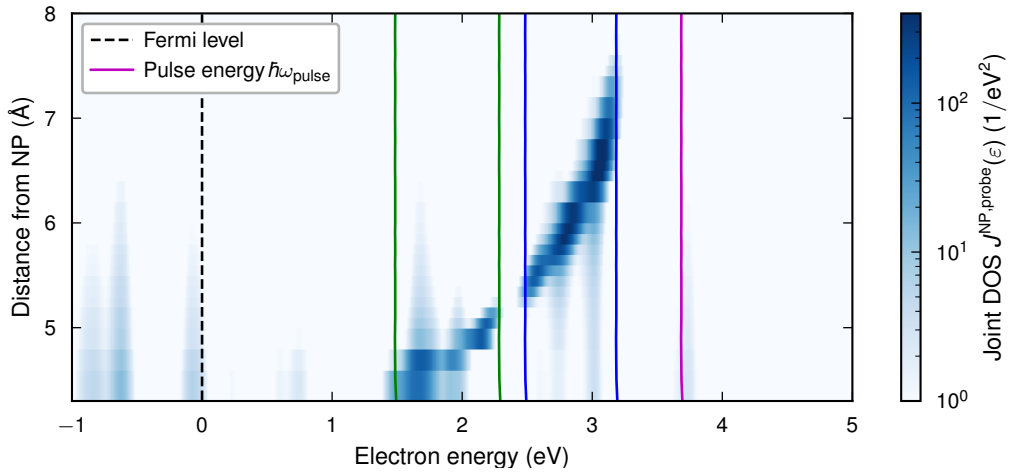


Figure 5.21: Probe orbital [111] on-top site joint density of states related to the direct hot-electron transfer process. This quantity shows how the hot-electron distribution (and hot-hole distribution shifted by $\hbar\omega_{\text{pulse}}$) would look if it only depended on the product of overlapping projected densities of state. The hot electrons are required to be between the Fermi level and the pulse energy, which are marked in the figure.

5.4 Summary

- The Ag₂₀₁ RTO + CO system was studied
- Binding energies of the NP+CO system were calculated for four sites as a function of distance, finding
 - Minima in binding energy around $d = 2.2 \text{ \AA}$ for corner and [111] on-top sites
 - Initial repulsion when approaching [111] fcc and [100] hollow sites
- Probabilities of direct hot-electron and hot-hole transfer were determined as a function of distance
 - Direct hot-electron transfer around $\sim 1 - 2\%$ for wide range of distances. Sensitive to site and choice of xc -functional
 - Direct hot-hole transfer at most 0.3% , decaying with distance
- Found that HC distributions (and consequently transfer probabilities) are explained by alignment of NP and molecular states
 - Hybridization important for distance dependence
- As proof-of-concept a probe orbital consisting of a harmonic-like potential was demonstrated
 - The same type of relations regarding PDOS alignment as for a CO molecule are observed

6

Conclusion

In this thesis optical and photocatalytical properties of Ag NPs have been studied. For a sequence of thermodynamically stable truncated octahedron-like NPs between 13 and 586 atoms in size, the ground state energies and photoabsorption spectra were computed. Confirming previous results obtained with an EAM potential, the PBE ground state energies were found to closely follow a third degree polynomial in $N^{-1/3}$. While the EAM potential predicted regular truncated octahedra to be lower in energy compared to the fit than other structures, the relative PBE energies were found to be lower for some of the rugby-like structures. From the calculated photoabsorption spectra the LSPR peak frequencies were found to be linear in $N^{-1/3}$ above $N \geq 201$, for both regular and irregular structures.

Binding energies as a function of distance were calculated for the Ag₂₀₁ RTO and a CO molecule. Out of the four considered sites of CO adsorption on the NP, the corner site exhibited the strongest binding, followed by the [111] on-top site. The [111] fcc and [100] hollow sites showed initial repulsion on CO approach.

For the same NP+CO system direct hot-electron and hot-hole transfer probabilities were calculated as a function of distance. The system was excited by a laser pulse tuned to the LSPR frequency. The two most strongly binding sites were considered. The direct hot-electron transfer process was found to occur with a probability of $\sim 1 - 2\%$ for wide range of distances. The particular value at a certain distance was sensitive to site and choice of xc -functional. The direct hot-hole transfer process was at most 0.3% probable, its probability decreasing with increasing distance.

It was found that the distribution of hot-electrons and hot-holes in the direct transfer processes was primarily determined by the alignment of molecular and NP projected densities of state (PDOS). In particular there must be a donor state in one PDOS and an acceptor state in the other, with their energy difference equal to the energy of the pulse. Both the HOMO and LUMO state of the molecule hybridized at small distances, spreading out over a range of energies. As the particular energies of the hybridized LUMO state depended on site and choice of xc -functional, also the hot-electron transfer showed this dependence. The energies of the hybridized HOMO state were less dependent on those factors, thus yielding a uniform distance dependence of the hot-hole transfer probability.

These findings imply that possible hot-carrier can be engineered by tuning the LSPR frequency (by changing NP size, shape, environment and composition), and surface electronic structure (by strain or alloying) to enhance or inhibit hot-electron or hot-hole transfer to certain molecular orbitals.

Bibliography

- [1] M. A. Beuwer, M. W. J. Prins, and P. Zijlstra, *Stochastic Protein Interactions Monitored by Hundreds of Single-Molecule Plasmonic Biosensors*, *Nano Letters* **15**, 3507 (2015).
- [2] F. A. A. Nugroho *et al.*, *Metal–polymer hybrid nanomaterials for plasmonic ultrafast hydrogen detection*, *Nature Materials* **18**, 489 (2019).
- [3] P. Christopher, H. Xin, and S. Linic, *Visible-light-enhanced catalytic oxidation reactions on plasmonic silver nanostructures*, *Nature Chemistry* **3**, 467 (2011).
- [4] L. R. Hirsch *et al.*, *Nanoshell-mediated near-infrared thermal therapy of tumors under magnetic resonance guidance*, *Proceedings of the National Academy of Sciences* **100**, 13549 (2003).
- [5] U. Kreibig and M. Vollmer, *Optical Properties of Metal Clusters*, Springer Series in Materials Science No. 25 (Springer, Berlin, 1995).
- [6] C. F. Bohren, *How can a particle absorb more than the light incident on it?*, *American Journal of Physics* **51**, 323 (1983).
- [7] C. Langhammer, B. Kasemo, and I. Zorić, *Absorption and scattering of light by Pt, Pd, Ag, and Au nanodisks: Absolute cross sections and branching ratios*, *The Journal of Chemical Physics* **126**, 194702 (2007).
- [8] K. L. Kelly, E. Coronado, L. L. Zhao, and G. C. Schatz, *The Optical Properties of Metal Nanoparticles: The Influence of Size, Shape, and Dielectric Environment*, *The Journal of Physical Chemistry B* **107**, 668 (2003).
- [9] A. B. Taylor and P. Zijlstra, *Single-Molecule Plasmon Sensing: Current Status and Future Prospects*, *ACS Sensors* **2**, 1103 (2017).
- [10] S. Linic, U. Aslam, C. Boerigter, and M. Morabito, *Photochemical transformations on plasmonic metal nanoparticles*, *Nature Materials* **14**, 567 (2015).
- [11] U. Aslam, V. G. Rao, S. Chavez, and S. Linic, *Catalytic conversion of solar to chemical energy on plasmonic metal nanostructures*, *Nature Catalysis* **1**, 656 (2018).
- [12] J. Ma and S. Gao, *Plasmon-Induced Electron–Hole Separation at the Ag/TiO₂ (110) Interface*, *ACS Nano* **13**, 13658 (2019).
- [13] P. V. Kumar *et al.*, *Plasmon-Induced Direct Hot-Carrier Transfer at Metal–Acceptor Interfaces*, *ACS Nano* **13**, 3188 (2019).
- [14] P. V. Kumar, T. P. Rossi, M. Kuisma, P. Erhart, and D. J. Norris, *Direct hot-carrier transfer in plasmonic catalysis*, *Faraday Discussions* **214**, 189 (2019).
- [15] E. Runge and E. K. U. Gross, *Density-Functional Theory for Time-Dependent Systems*, *Physical Review Letters* **52**, 997 (1984).

- [16] C. A. Ullrich and Z.-h. Yang, *A brief compendium of time-dependent density-functional theory*, Brazilian Journal of Physics **44**, 154 (2014), arXiv:1305.1388.
- [17] M. Kuisma *et al.*, *Localized surface plasmon resonance in silver nanoparticles: Atomistic first-principles time-dependent density-functional theory calculations*, Physical Review B **91**, 115431 (2015).
- [18] J. M. Rahm and P. Erhart, *Beyond Magic Numbers: Atomic Scale Equilibrium Nanoparticle Shapes for Any Size*, Nano Letters **17**, 5775 (2017).
- [19] R. M. Martin, *Electronic Structure: Basic Theory and Practical Methods*, 1st ed. (Cambridge University Press, 2004).
- [20] P. Hohenberg and W. Kohn, *Inhomogeneous Electron Gas*, Physical Review **136**, B864 (1964).
- [21] W. Kohn and L. J. Sham, *Self-Consistent Equations Including Exchange and Correlation Effects*, Physical Review **140**, A1133 (1965).
- [22] P. A. M. Dirac, *Note on Exchange Phenomena in the Thomas Atom*, Mathematical Proceedings of the Cambridge Philosophical Society **26**, 376 (1930).
- [23] F. Bloch, *Bemerkung zur Elektronentheorie des Ferromagnetismus und der elektrischen Leitfähigkeit*, Zeitschrift für Physik **57**, 545 (1929).
- [24] J. P. Perdew and Y. Wang, *Accurate and simple analytic representation of the electron-gas correlation energy*, Physical Review B **45**, 13244 (1992).
- [25] J. P. Perdew, K. Burke, and M. Ernzerhof, *Generalized Gradient Approximation Made Simple*, Physical Review Letters **77**, 3865 (1996).
- [26] O. Gritsenko, R. van Leeuwen, E. van Lenthe, and E. J. Baerends, *Self-consistent approximation to the Kohn-Sham exchange potential*, Physical Review A **51**, 1944 (1995).
- [27] J. P. Perdew and M. Levy, *Physical Content of the Exact Kohn-Sham Orbital Energies: Band Gaps and Derivative Discontinuities*, Physical Review Letters **51**, 1884 (1983).
- [28] M. Kuisma, J. Ojanen, J. Enkovaara, and T. T. Rantala, *Kohn-Sham potential with discontinuity for band gap materials*, Physical Review B **82**, 115106 (2010).
- [29] J. Yan, K. W. Jacobsen, and K. S. Thygesen, *First-principles study of surface plasmons on Ag(111) and H/Ag(111)*, Physical Review B **84**, 235430 (2011).
- [30] J. Yan, K. W. Jacobsen, and K. S. Thygesen, *Conventional and acoustic surface plasmons on noble metal surfaces: A time-dependent density functional theory study*, Physical Review B **86**, 241404 (2012).
- [31] S. L. Dudarev, G. A. Botton, S. Y. Savrasov, C. J. Humphreys, and A. P. Sutton, *Electron-energy-loss spectra and the structural stability of nickel oxide: An LSDA+U study*, Physical Review B **57**, 1505 (1998).

-
- [32] I. Vasiliev, S. Ögüt, and J. R. Chelikowsky, *Ab Initio Excitation Spectra and Collective Electronic Response in Atoms and Clusters*, *Physical Review Letters* **82**, 1919 (1999).
- [33] I. Vasiliev, S. Ögüt, and J. R. Chelikowsky, *First-principles density-functional calculations for optical spectra of clusters and nanocrystals*, *Physical Review B* **65**, 115416 (2002).
- [34] J. J. Mortensen, L. B. Hansen, and K. W. Jacobsen, *Real-space grid implementation of the projector augmented wave method*, *Physical Review B* **71**, 035109 (2005).
- [35] J. Enkovaara *et al.*, *Electronic structure calculations with GPAW: A real-space implementation of the projector augmented-wave method*, *Journal of Physics: Condensed Matter* **22**, 253202 (2010).
- [36] M. Walter *et al.*, *Time-dependent density-functional theory in the projector augmented-wave method*, *Journal of Chemical Physics* **128**, 244101 (2008).
- [37] A. H. Larsen, M. Vanin, J. J. Mortensen, K. S. Thygesen, and K. W. Jacobsen, *Localized atomic basis set in the projector augmented wave method*, *Physical Review B* **80**, 195112 (2009).
- [38] T. P. Rossi, M. Kuisma, M. J. Puska, R. M. Nieminen, and P. Erhart, *Kohn–Sham Decomposition in Real-Time Time-Dependent Density-Functional Theory: An Efficient Tool for Analyzing Plasmonic Excitations*, *Journal of Chemical Theory and Computation* **13**, 4779 (2017).
- [39] A. H. Larsen *et al.*, *The atomic simulation environment—a Python library for working with atoms*, *Journal of Physics: Condensed Matter* **29**, 273002 (2017).
- [40] P. E. Blöchl, *Projector augmented-wave method*, *Physical Review B* **50**, 17953 (1994).
- [41] P. Pulay, *Convergence acceleration of iterative sequences. the case of scf iteration*, *Chemical Physics Letters* **73**, 393 (1980).
- [42] P. L. Williams, Y. Mishin, and J. C. Hamilton, *An embedded-atom potential for the Cu–Ag system*, *Modelling and Simulation in Materials Science and Engineering* **14**, 817 (2006).
- [43] S. Raza, W. Yan, N. Stenger, M. Wubs, and N. A. Mortensen, *Blueshift of the surface plasmon resonance in silver nanoparticles: Substrate effects*, *Optics Express* **21**, 27344 (2013).
- [44] P. M. Diehm, P. Ágoston, and K. Albe, *Size-Dependent Lattice Expansion in Nanoparticles: Reality or Anomaly?*, *ChemPhysChem* **13**, 2443 (2012).

